POLITECNICO DI TORINO

Master's Degree in Electronic Engineering

Master's Degree Thesis

Design of an RF Component for In-Band Full-Duplex Systems

Supervisors
Prof. Giuseppe VECCHI
Politecnico di Torino

Prof. Danilo ERRICOLO
University of Illinois Chicago

Candidate
Francesco PRESTA

July 2025

ACKNOWLEDGMENTS

I want to thank my parents for their unconditional love and support in my academic journey. Their sacrifices and faith are the foundation of everything I achieved.

I am also thankful to my friends for the shared moments of joy that helped relieve the stress during the most challenging times. A special thanks to my girlfriend whose patience and understanding helped me to stay focused and motivated.

I sincerely acknowledge my research group and advisor for their invaluable guidance and for providing me with the opportunity to grow in a stimulating environment.

FP

TABLE OF CONTENTS

LIST OF TABLES

LIST OF FIGURES

LIST OF FIGURES (continued)

FIGURE **PAGE**

LIST OF ABBREVIATIONS

UIC	University of Illinois at Chicago
IBFD	In-Band Full-Duplex
STAR	Simultaneously Transmit And Receive
SIC	Self Interference Cancellation
CW	Clockwise
CCW	Counterclockwise

SUMMARY

This work explores the design, optimization, and practical implementation of an advanced rat-race coupler with enhanced bandwidth and isolation performances for self-interference cancellation (SIC) in in-band full-duplex systems. The component is positioned at the antenna interface to effectively mitigate the self-interference signal from the received signal, exploiting the inherent signal-processing properties of the component. To address these challenges, the novel approach proposed consists of the implementation of Chebyshev multi-section transformers in the component structure, with an improvement of 30% in operative bandwidth and doubling the isolation bandwidth. This thesis starts with a comprehensive theoretical analysis of the 180-hybrid coupler, with particular emphasis on even and odd mode analysis and the delicate amplitude and phase balance needed for optimal isolation.

The proposed structure is validated both with schematic and EM full-wave simulations using Keysight Advanced Design System (ADS). The optimized microstrip implementation is finally realized on a Rogers RO4003C substrate and measured, demonstrating a superior isolation level and bandwidth with respect to a conventional structure.

This work contributes to advancing the SIC capabilities at the antenna interface by relying on passive components only. The proposed solution reduces the dependence on complex active cancellation techniques, supporting the goal of reducing the self-interference signal and enabling IBFD communication for next-generation wireless technologies.

CHAPTER 1

INTRODUCTION

1.1 In-Band Full-Duplex Overview

In wireless networks, bi-directionality in communications is usually achieved through half-duplex schemes such as Time Division Duplex (TDD) and Frequency Division Duplex (FDD) [1]. The first utilizes a single channel alternating transmission and reception in different time slots, whereas the second uses two separate channels for transmission and reception. FDD suffers from inefficient spectrum utilization and does not adapt well to dynamic traffic loads since the frequency bands allocated for transmission and reception are fixed. On the other hand, TDD introduces an inherent latency in communication and requires precise timing synchronization. Today, FDD is used in GSM, LTE, 5G, and satellite communications, while TDD is used in LTE, 5G, Bluetooth, and WiFi. Both techniques exhibit low efficiency and throughput, making them unsuitable for future high-speed communications demands.

In-band full-duplex (IBFD) systems enable simultaneous transmission and reception on the same channel, maximizing spectral efficiency and throughput while minimizing latency [2][3]. IBFD is already implemented in some military radios [4][5] and is a promising core solution for future communication standards such as 6G [6][7] and WiFi 7 [8].

The main technical challenge for implementing IBFD communication is the issue of self-interference (SI) that arises from the coupling between the transmitted and received signals.

Specifically, the transmitted signal exhibits high power, and the portion that leaks on the reception channel obscures the signal of interest, potentially leading to a saturation of the receiver.

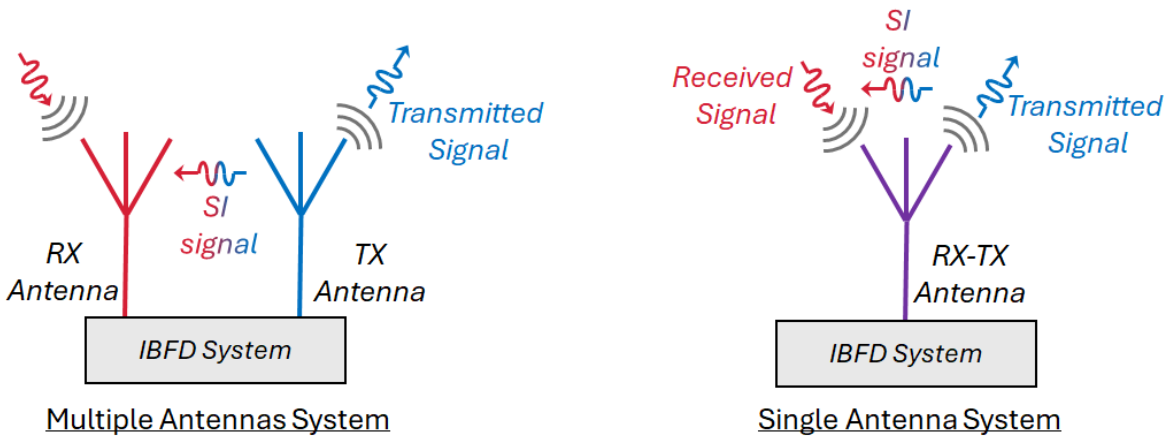

Figure 1: Self-Interference Illustration

The aim is to reduce the SI close to the noise floor, requiring an isolation between transmit and receive channels above 100 dB [2]. Achieving and maintaining this level of self-interference cancellation (SIC) in real-time requires the implementation of multiple design strategies along the RF chain, involving the antenna/propagation domain, the analog domain, and finally, the digital domain.

Modern processors enable the implementation of complex algorithms to effectively cancel nonlinearities, phase noise, and IQ imbalance. These algorithms can also adapt to changing environments without requiring excessive hardware complexity. As a result, cancellation in the digital domain is preferred once the signal is digitized by the ADC. The role of propagation and analog domain technique is then to attenuate as much as possible the SI component in order to minimize the ADC quantization error, which depends on the difference between the dynamic range of the signal of interest and that of the SI at the ADC input [3].

Over the past few years, the interest in IBFD has grown, with many research activities involved, the *IEEE Transactions on Antennas and Propagation* that published the special issue in [2], and the inaugural first issue of *IEEE Journal of Special Topics in Electromagnetics, Antennas and Propagation* [9] on this topic. The research group of Prof. Erricolo, in the Andrew Electromagnetic Laboratory at the University of Illinois Chicago (UIC), has provided multiple contributions to IBFD, including the design of antennas that leverage field cancellation to improve inherent SIC capabilities [10][11], various RF circuits for improving SIC [12] [13], a book chapter [14], and the work in [15] that led to the patent [16]. In particular, contributions where given to circularly polarized microstrip antennas [17] [18] [19] [20], and, in this context, the research activity carried out in this thesis aims to the design of a rat-race use to enhance the inherent SIC performance as part of the antenna system in [21].

The wide-band patch array antenna proposed in [21] consists of three circularly polarized elements, with one transmitting antenna placed between two receiving antennas. The current distribution and the position of the antennas are selected to create a null-field region between

the two RX antennas, allowing for SIC level below -50 dB between 5.4 GHz and 5.7 GHz, just with the antenna itself. The 180-hybrid designed in this thesis exhibits wide-band behavior and enhanced isolation level within the operating range from 5 GHz to 6 GHz. When this is connected to the two RX antennas, the SIC performance further improve, with reduction of the SIC level below -60 dB in a 300 MHz band within 5.4 GHz and 5.7 GHz, and below -50 dB in a 700 MHz band between 5.1 GHz and 5.8 GHz.

1.2 Self-Interference Cancellation Level

As mentioned in the previous section, for an effective demodulation of the received signal, the Self-Interference component has to be attenuated by 100 dB. The aim of this section is to provide a justification for this high level of suppression required.

The receiver architectures are designed to deal with a noise floor whose power ranges from 80 dBm to 140 dBm [22] depending on temperature and bandwidth. By reducing the power of the SI signal below this level, it becomes negligible compared to the inherent noise floor.

The maximum transmitting power for WiFi (802.11n/ac/ax) is limited to 20 dBm (100 mW) in the 2.4 GHz band [23] and 23 dBm (200 mW) in the 5 GHz band [24], with an average power in the range between 15 dBm and 20 dBm (from 30 mW to 100 mW). The maximum transmitting power for LTE/5G UE is limited to 23 dBm (200 mW) [25][26]. As a result, in most of the laboratory experiments on IBFD systems, the transmitted power is in the 0 dBm to 20 dBm range [27][28].

Assuming a SI signal of 10 dBm (-20 dB) having the same power of the transmitted signal, as in single antenna IBFD systems, to attenuate the SI component by 10dB below the noise floor of -80 dBm (-110 dB), the amount of SIC required is:

$$SIC = P_{TX} \; - \; P_N \; - \; 10\;dB = -20\;dB \; - \; (\; -110\;dB\;) \; - 10\;dB \; = 100\;dB \tag{1.1}$$

This proves that the minimum amount of SIC required for an effective demodulation of the incoming signal is -100 dB. In common IBFD systems, an attenuation of -30 dB is obtained in the propagation domain, -30 dB in the analog domain and -40 dB in the digital domain.

The antenna system proposed in [21], combined with the rat-race combiner designed in this thesis, allow for SIC performance better than -60 dB in the propagation domain. This makes possible to obtain a suppression level of the SI signal even higher that 100 dB when also accounting the SIC techniques in the analog and digital domain. This contribute to make IBFD more feasible for future applications.

1.3 Structure of the thesis

This this thesis begins with a brief introduction to the context of In-Band Full-Duplex systems, providing an overview on the relevance and application of the component designed in this work. Chapter 2 presents an overview of the theoretical background involved in the design, followed by an explanation of the design workflow and of the simulations performed. The theoretical sections focus on the key concept for this research.

Chapter 3 discuss about the design of a rat-race coupler with the desired characteristics of bandwidth and isolation. In the first part there is a step-by step implementation of the design, with both theoretical explanations and a comparison of the obtained results with a conventional rat-race ring. In the same chapter follows the microstrip implementation, the layout generation and the results of the EM full-wave simulations

Chapter 4 discuss the fabrication and measurement results of the physical component. Finally, this thesis concludes with a summary of the research with suggestions for potential directions for future works.

CHAPTER 2

BACKGROUND

2.1 Multi-Section Transformer

The purpose of multi-section transformers is to provide wide-band impedance matching between the source and the load. Compared to quarter-wave transformers, which can match an arbitrarily real load to any transmission line (assuming lossless conditions) but only over a narrow frequency range, multi-section transformers implement a gradual impedance transition that reduces the reflections due to the frequency-dependent impedance variations. This approach maintains the input impedance around the design value and minimizes the reflection coefficient across a wider frequency band.

The aim of the following mathematical demonstration is to extract the frequency-dependent polynomial expression of the reflection coefficient and map it to the desired response, as illustrated in [22].

Let us consider a multi-section transformer composed of N equal-length transmission lines, with monotonically increasing characteristic impedances as in Figure 2. Referring to the *small reflection approximation*, we assume the transition between characteristic impedance to be very gradual, such that $Z_i \approx Z_{i-1}$. As a result, the mismatch at each interface is minimal and most of the incident power is transmitted at the discontinuity. An incident unit-amplitude wave propagating along the transformer experiences reflections at each interface, with each reflected

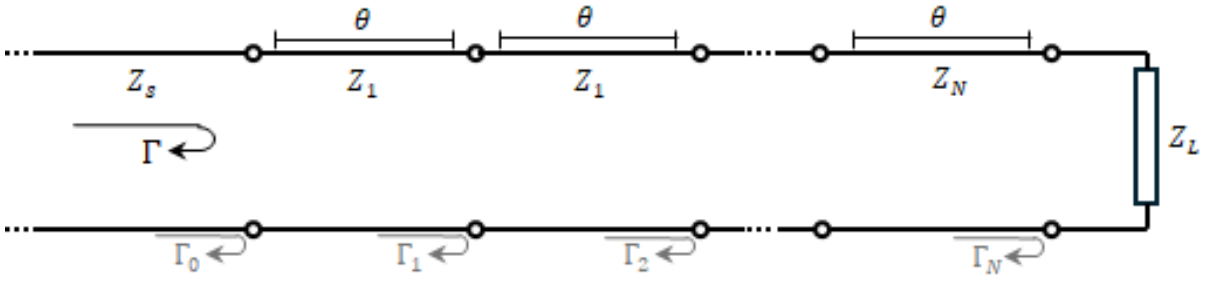

Figure 2: Reflections in a multisection transformer matching the real load Z_L with the source chatacteristic impedance Z_s

wave travels back while most of the power is transmitted forward, as previously explained. The total reflected wave is then the sum of the small reflections on the N-interfaces, each with a phase accumulation equal to twice the electrical distance from the interface and the source due to the round-trip. An approximated expression for the overall reflection coefficient $\Gamma = \frac{V^-}{V^+}$ is given in Equation 2.1 [22]. It should be noted that, the reflection produced on each interface is itself an infinite sum of internal reflections within the section; however, due to the small reflection hypothesis, the amplitude of these high order terms decreases rapidly, making the first order reflections the dominant contributes to the total Γ.

$$\Gamma(\theta) = \Gamma_0 + \Gamma_1 e^{-2j\theta} + \Gamma_2 e^{-4j\theta} + ... + \Gamma_N e^{-2jN\theta} \qquad \text{with} \quad \Gamma_i = \frac{Z_{in,i+1} - Z_i}{Z_{in,i+1} + Z_i} \tag{2.1}$$

Assuming also that the reflection coefficients are symmetrical along the transformer ($\Gamma_0 = \Gamma_N, \Gamma_1 = \Gamma_{N-1},\ ...$)), still maintaining the monotonical variation of the characteristic impedances, Equation 2.1 can be manipulated into Equation 2.2, as derived in [22].

$$\begin{aligned}\Gamma(\theta) &= \Gamma_0(1+e^{-j2\theta}) + \Gamma_1(^{-j2\theta}+e^{-j2(N-1)\theta}) + \Gamma_2(e^{-j4\theta}+e^{-j2(N-2)\theta}) \ + \ ... = \\ &= 2e^{-jN\theta}\big[\Gamma_0(e^{jN\theta}+e^{-jN\theta}) + \Gamma_1(e^{j(N-2)\theta}+e^{-j(N-2)\theta})\big] + \ ... = \\ &= 2e^{-jN\theta}\Big[\Gamma_0\cos N\theta + \Gamma_1\cos(N-2)\theta + \Gamma_n\cos(N-2n)\theta + \begin{cases} \frac{1}{2}\Gamma_{N/2} & \textit{for } N \textit{ even} \\ \Gamma_{(N-1)/2}\cos\theta & \textit{for } N \textit{ odd} \end{cases}\Big]\end{aligned} \tag{2.2}$$

By properly selecting the Γ_n and the number of sections N it is possible to synthetize ant reflection coefficient response as a function of the frequency (θ). In the next subsection will be explained how to synthetize the Chebyshev passband response

2.1.1 Multisection Transformer with Chebyshev Profile

Chebyshev response optimize bandwidth compromising the the flatness of the band-pass response, that presents some ripple. Chebyshev polynomials $T_n(x)$ are a family of orthogonal polynomials whose amplitude oscillates within passband, corresponding to the range $-1 \leq x \leq 1$, and exponentially increases in the stopband, for $|x| > 1$. As shown in Figure 3, the rate of increase in the stop band becomes steeper with the polynomial order n. The first four Chebyshev polynomials and the formula to recursively derive higher-order polynomials are in Equation 2.3 [18].

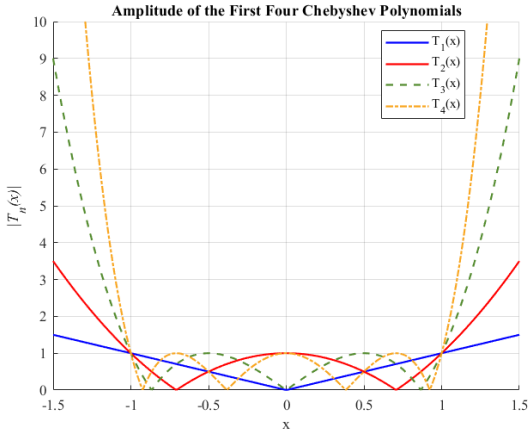

Figure 3: Chebyshev Polynomials Amplitude as function of x

$$
\begin{aligned}
T_1(x) &= x \\
T_2(x) &= 2x^2 + 1 \\
T_4(x) &= 8x^4 - 8x^2 + 1 \\
&\vdots \\
T_n(x) &= 2x \cdot T_{n-1}(x) - T_{n-2}(x)
\end{aligned}
\tag{2.3}
$$

Assuming $x = \cos\theta$, in the pass-band ($|x| < 1$) it holds $T_n(x) = T_n(\cos\theta) = \cos^n\theta$, while in the stop-band ($|x| > 1$) we have $T_n(x) = \cosh\left(n \cdot \cosh^{-1} x\right)$. To set map the pass-band to the desired frequency interval corrisponding to $\theta \in [\theta_m\,; \pi - \theta_m]$ we make:

$$\begin{aligned} x = 1 \qquad \text{for} \quad \theta = \theta_m \quad &\Longrightarrow \quad \cos\theta_m = 1 \\ x = -1 \qquad \text{for} \quad \theta = \pi - \theta_m \quad &\Longrightarrow \quad \cos\left(\pi - \theta_m\right) = 1 \end{aligned} \tag{2.4}$$

This is accomplished by substituting $x = \frac{\cos\theta}{\cos\theta_m} = \sec\theta_m \cos\theta$ into Equation 2.3, obtaining Equation 2.6 [22].

$$\begin{aligned} T_1(\sec\theta_m \cos\theta) &= \sec\theta_m \cos\theta, \\ T_2(\sec\theta_m \cos\theta) &= \sec^2\theta_m \cos 2\theta + \left(\sec^2\theta_m - 1\right) \\ T_3(\sec\theta_m \cos\theta) &= \sec^3\theta_m \cos(3\theta) + \left(\sec^3\theta_m - 3\sec\theta_m\right)\cos\theta \\ T_4(\sec\theta_m \cos\theta) &= \sec^4\theta_m \cos 4\theta + \left(4\sec^4\theta_m - 4\sec^4\theta_m\right)\cos 2\theta + \left(3\sec^4\theta_m - 4\sec^2\theta_m + 1\right) \end{aligned} \tag{2.5}$$

The Chebyshev response of the multisection transformer is obtained by mapping the reflection coefficients in Equation 2.2 to the coefficients of the cosine terms in Equation 2.5 as in Equation 2.7. Once the reflected coefficients are known, the corresponding values of characteristic impedance are calculated by inverting Equation 2.1

$$\begin{aligned} \Gamma(\theta) &= 2e^{-jN\theta}\big[\Gamma_0 \cos N\theta + \Gamma_1 \cos\left(N-2\right)\theta + \Gamma_n \cos\left(N-2n\right)\theta + \begin{cases} \frac{1}{2}\Gamma_{N/2} & \textit{for } N \textit{ even} \\ \Gamma_{(N-1)/2}\cos\theta & \textit{for } N \textit{ odd} \end{cases} \\ &= \quad A e^{-jN\theta}\, T_n(\sec\theta_m \cos\theta) \end{aligned} \tag{2.6}$$

The value of θ ranges from 0 to θ_m within the pass band and exceed θ_m in the stopband.

Notice that, at $\theta = 0$, which corresponds to the lower frequency limit, all the phase terms $e^{-j2k\theta}$ in Equation 2.2 are unity and maximize their contribution. As a consequence, the overall reflection coefficient ($\Gamma(0)$) also reaches its maximum as it appears as the sum of all the interface reflections: $\Gamma(0) = \Gamma_0 + \Gamma_1 + \ ... \ + \Gamma_N$. The constant A then represents the peak in-band ripple and is evaluated as expressed in Equation 2.7.

$$A = \frac{\Gamma_{\max}}{T_N(\sec\theta_m)} \tag{2.7}$$

The results obtained in this section are an approximation since they rely on *small reflection approximation*. These provide a valuable insight into the working principle and are general enough for the design of a transformer with an arbitrary maximum ripple level. Exact results can be found in tables in [22] and [29].

2.1.2 Comparison of Multisection Transformers Profiles

The previous section discussed the implementation of the Chebyshev profile as the frequency-dependent reflection coefficient o a multisection transformer, however, in principle any continuous impedance profile can be implemented, untill this provide physically realizable characteristic impedances $Z(x) > 0$. In this section we discuss about the performances of the most common impedance transformer profiles, namely Chebyshev, Binomial (Maximally Flat) and Klopfenstein profiles.

The Chebyshev profile is widely adopted when stopband attenuation and passband return loss are priorities. It provides a fast transition from passband to stopband and support a

wideband response at the cost of an in-band ripple. However, the ripple peak amplitude can be effectively controlled to meet the design constraints, as shown in the previous section [22][29].

The Binomial/Maximally-Flat profile is preferred when in-band flatness is the main concern. It allows for no ripple within the pass-band but suffers from narrower bandwidth and slower roll off in stop-band, making it not appealing for wide-band designs[22][29].

Finally, the Klopfenstein profile provides the best trade off between length and performance, offering the shortest transformer for a specified maximum reflection coefficient and fast roll-off in stop-band. The main drawback is the high fabrication complexity and the high sensibility to manufacturing tolerances, since it requires either a continuous taper or many finite discrete steps to accurately approximate the profile. In addition, unlike Chebyshev profile, it does not offer an explicit control for the in-band ripple[22][29][30].

A summary of the performance comparison between the different transformer profiles is provided in Table I.

TABLE I: COMMON MULTISECTION TRANSFORMERS PROFILES

Criterion	**Chebyshev**	**Binomial**	**Klopfenstein**
Passband Reflection	Controlled ripple	Ripple-free	Controlled
Stopband Attenuation	Fast, exponential	Slow, polynomial	Fast
Roll-off Speed	Very steep	Gentle	Steep
Bandwidth	Wideband	Narrower than Chebyshev	Wideband
Ripple Control	Explicit	-	No explicit control
Transformer Length	Moderate	Longest	Shortest
Fabrication Complexity	Medium	Low	High
Sensitivity to Tolerances	Moderate	Low	High
Design Complexity	Medium	Low	High

2.1.3 Effect of Section Length in Multi-Section Transformers

In multi-section transformers, the typical choice for the section length is $l = \lambda/4$, not for its strong impedance transformation capabilities but also for the beneficial effect associated with the accumulation of phases.

As discussed in the previous section, each impedance discontinuity generates a reflected wave that propagates back toward reaching the source with an accumulated phase shift equal

to twice the electrical length of its path due to the round-trip. As a result, the phase difference at the source between two reflections generated by adjacent component is equal to:

$$\Delta\phi_{i,i-1} = 2\beta l \cdot i - 2\beta l \cdot (i-1) = 2\beta l \tag{2.8}$$

In the case of $l = \lambda/4$, Equation 2.8 becomes:

$$\Delta\phi_{i,i-1} = 2\left(\frac{2\pi}{\lambda}\right) \cdot \frac{\lambda}{4} = \pi \tag{2.9}$$

As a result, the reflections from adjacent sections are out of phase and interfere destructively, reducing the overall reflection coefficient and increasing the steepness steepness of the stop-band attenuation. As the value of l changes for both larger and smaller values of $\lambda/4$, the reflections gets further from the out-of phase consdition and the cancellation effect reduces. The limit condition occurs either as $l \longrightarrow 0$ or at $l = \lambda/2$, where $\Delta\phi_{i,i-1} = 0$ and the reflections interfere constructively, significantly worsening the reflection coefficient roll-off. This behavior is periodic with respect to the section length l, with destructive interferences occurring for odd multiples of $\lambda/4$ and constructive interferences for odd multiple of $\lambda/2$. Understanding this periodicity is essential to find the optimal trade off between the overall transformer length and the performance, especially in the case of integrated layouts as the one of the 180-hybrid in this thesis.

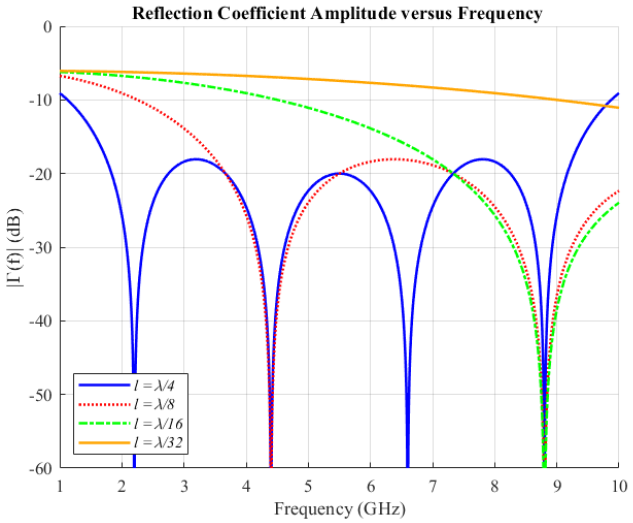

Figure 4: Effect of section length variation on the reflection coefficient amplitude of a five-section Chebyshev transformer as a function of frequency

2.1.4 The Fano-Bode Criterion

The Bode-Fano criterion sets a fundamental theoretical limit on the minimum magnitude of the reflection coefficient that can be achieved with an arbitrary, passive matching network. In other words, for a given load, the broader the desired matching bandwidth, the maximum reflection coefficient peaks in the band [22][31]. Bode-Fano's criterion in Equation 2.10[32]

defines the optimum result in terms of bandwidth and reflection coefficient amplitude that can be ideally archived and approximated in practice but not surpassed.

$$\int_0^\infty \ln \frac{1}{|\Gamma(\omega)|^2} \, \frac{d\omega}{\omega^2} \leq \frac{\pi}{Q} \tag{2.10}$$

This inequality implies that zero reflection across the bandwidth is impossible and that perfect matching can only be obtained at a finite number of discrete frequencies only [22].

In the case of the multisection transformer, increasing the number and length of the sections leads to an increase of matching bandwidth with a decrease of the quality factor Q and, finally, a higher minimum in-band reflection coefficient, according to the Bode-Fano criterion. A flatter but zero in-band reflection coefficient is then the direct consequence of the wideband matching provided.

2.2 Microstrip-line Theory

Microstrip lines are one of the most widely used forms of planar transmission lines in modern RF/microwave circuits, especially for their ease of manufacturing and integration with active and passive components. For mass production, they are typically fabricated with standard photolithography and etching processes, ensuring cost-effectiveness and up-to-micrometer precision essential for high-frequency applications. For fast prototyping they can be fabricated using CNC machines, however, this solution is generally not cost-effective and allows for a significantly lower resolution compared to etching techniques.

Figure 5 illustrates the cross-section of a microstrip line. This is composed of a conductor strip with width W and thickness t, that lies on top of a dielectric substrate with thickness h and relative permittivity ϵ_r. The substrate itself lies on a grounded metal layer known as the ground plane.

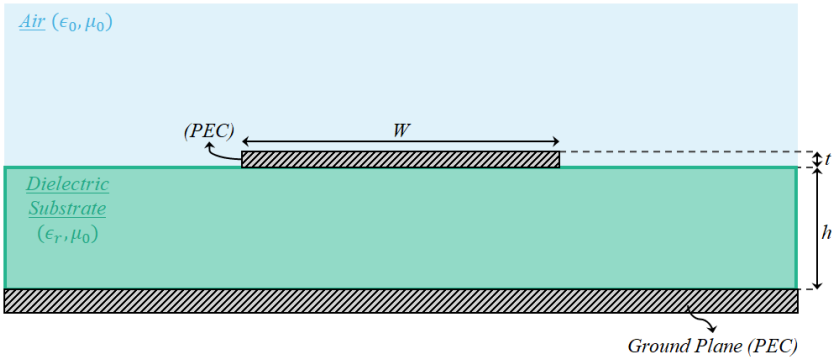

Figure 5: Microstrip geometrical dimensions represented on the cross-section plane

Assuming the strip and the ground plane made of perfect electric conductor (PEC), the boundary condition imposes that the tangent component of the electric field at the conductor surface is null; as a result, the electric field lines arise and terminate on the two conductors and are normal to the surface at the interface. On the contrary, the boundary conditions of the magnetic field require the normal component to be null, resulting in the magnetic field lines circulating around the conductor always parallel to the surface. The portrait of electric and magnetic fields in the microstrip-cross section is shown in Figure 6.

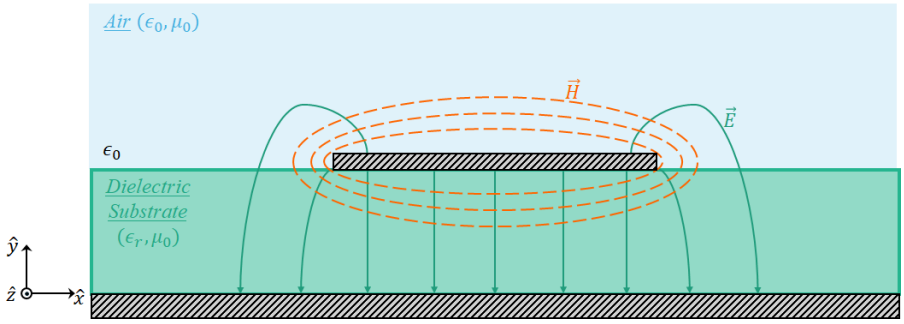

Figure 6: Electric and Magnetic field lines represented on the cross-section plane of the microstripline

The conductor strip is positioned between two means: the air above, with permittivity ϵ_0, and the dielectric below, with relative dielectric permittivity ϵ_r. As a consequence, the electric field is not contained within a homogeneous and the electric field lines cross regions

with different permittivities and phase velocities $v_p = c_0/\sqrt{\epsilon_r}$. This phenomenon is known as *fringing* and causes in the longitudinal components (along $\hat{z}$ if the reference system in Figure 6 is considered) to be not null at the air-dielectric interface, making the propagation mode non-TEM. However, in most applications, the dielectric thickness is much smaller than the operating wavelength ($h/W \ll \lambda$), ensuring the longitudinal components to be much weaker if compared to the transverse ones Consequently, the propagation mode in a microstrip can be approximated to *quasi-TEM*, allowing the extension of TEM transmission lines theory to estimate key parameters, such as characteristic impedance [22] [33].

2.2.1 Effective permittivity and Characteristic Impedance

As explained before, under the hypothesis of $h/W \ll \lambda$, it is possible to approximate the hybrid TE-TM mode that propagates into the microstrip to a quasi-TEM. We can then consider the strip as floating inside a single mean (as TEM mode) with permittivity ($1 < \epsilon_{eff} < \epsilon_r$) known as *effective permittivity* and evaluated in Equation 2.11 [22] from the geometric characteristics of the microstrip.

$$\epsilon_{eff} = \frac{\epsilon_r + 1}{2} + \frac{\epsilon_r - 1}{2} \frac{1}{\sqrt{1 + \frac{2h}{W}}} \tag{2.11}$$

Once ϵ_r is calculated, the phase velocity and propagation constant can be evaluated as in Equation 2.12 [22], while the characteristic impedance as in Equation 2.13 [22].

$$v_p = \frac{c_0}{\sqrt{\epsilon_{eff}}} \qquad \beta = k_0\sqrt{\epsilon_{eff}} \tag{2.12}$$

$$Z_0 = \begin{cases} \frac{60}{\epsilon_{eff}} \ln\left(\frac{8h}{W} + \frac{W}{4h}\right) & \text{for } \frac{W}{d} \leq 1 \\ \frac{120\pi}{\sqrt{\epsilon_r}\left[\frac{W}{h} + 1.393 + 0.667 \ln\left(\frac{W}{h} + 1.444\right)\right]} & \text{for } \frac{W}{d} \geq 1 \end{cases} \tag{2.13}$$

The formulas for effective permittivity and characteristic impedance presented in Equation 2.11 and Equation 2.4 provide an approximation valid in quasi-static conditions only (low frequency). Even though we approximated the microstrip line to a quasi-TEM structure, we recall that the mode is actually an hybrid of TM and TE modes, so both the impedance and the effective permittivity variy with frequency. A frequency dependent effective permittivity implies a phase velocity that changes with frequency and a dispersive behavior. In other words the components of a broadband signal will reach the end of the line at different times creating a distortion of the input signal. Approximated formulas are not suitable since these are not accurate enough over a sufficiently wide frequency range, so numeric models are usually preferred, as the ones proposed in [34] and [35].

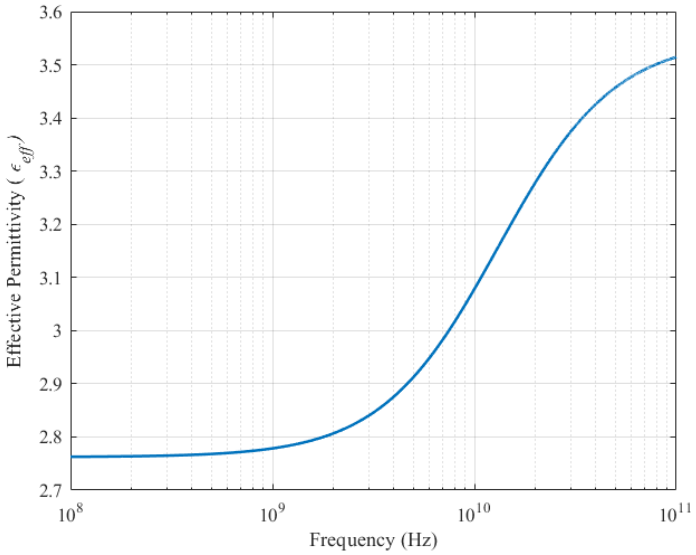

Figure 7: Frequency behavior of effective permittivity in a microstrip line with $W = 3$ mm, $L = 32$ mil, $\epsilon_r = 3.55$, and $t = 35\ \mu$m

Figure 7 shows the plot of the effective permittivity as a function of the frequency considering the dispersive model in [36];

2.2.2 Losses in Microstrip-line

In a microstrip line the attenuation is the sum of different components, the most prominent are the conductor attenuation and the dielectric attenuation. Conductor attenuation arise from the finite conductivity of the conductor (σ) which makes the strip and the ground plane. As the frequency increases, current tends to concentrate close to the surface of the conductor rather than distributing uniformly across the cross section (*skin effect*), resulting in an increase of sur-

face resistance (R_S). The attenuation of the wave due to the conductor losses is approximately given by Equation 2.14 [22].

$$\alpha_c = \frac{R_s}{Z_0 W} \quad \Big[Np/m\Big] \qquad \text{where} \quad R_s(f) = \sqrt{\frac{\pi f \mu}{\sigma}} \quad \Big[\Omega/\square\Big] \tag{2.14}$$

Conversely, dielectric attenuation (α_d) is related to the energy dissipation phenomena that take place in a real dielectric. In particular, when an electric field is applied, the dipoles align storing energy and release energy when the electric field is no more present, all without losses. In a real dielectric, instead, part of the energy provided by the field is dissipated by heat due to molecular frictions and relaxation delays. These energy losses are taken into account by the imaginary part of the permittivity (ϵ''), while the real part (ϵ') accounts for the energy stored. An approximation of the attenuation resulting due to dielectric losses is given by Equation 2.15 [22], in which the term $\tan\delta = \frac{\epsilon''}{\epsilon'}$ is known as *loss tangent*.

$$\alpha_d = \frac{k_0 \epsilon_r \big(\epsilon_{eff} - 1\big)}{2\sqrt{\epsilon_{eff}}\big(\epsilon_r - 1\big)} \tan\delta \quad \Big[Np/m\Big] \tag{2.15}$$

Considering Equation 2.14 and Equation 2.15, the dielectric attenuation grows as f (linearly with frequency) while the conductor attenuator grows as $\sqrt{f}$. The dielectric attenuation is then expected to prevail at low frequencies while the conductor losses dominate at higher frequencies. The behavior just depicted can be observed in Figure 8 [36].

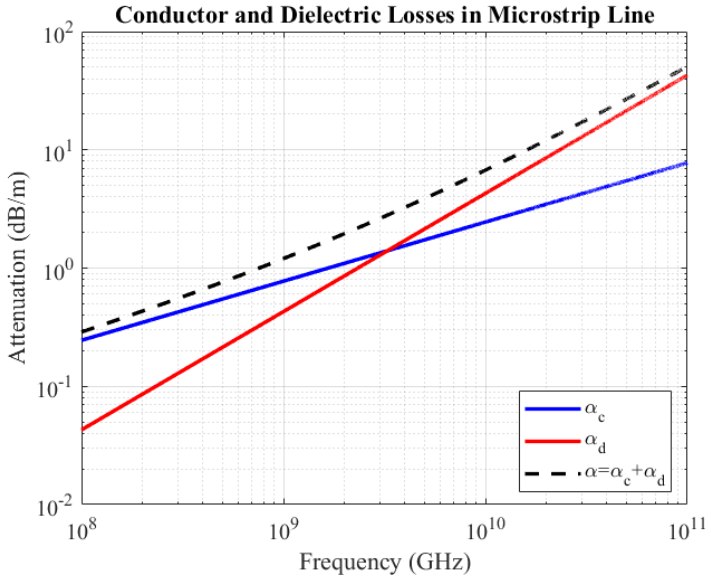

Figure 8: Frequency behavior of dielectric, conductor and overall attenuation in a microstrip line with $W = 1.8$ mm, $L = 32$ mil, $W = 35$ μm, $\epsilon_r = 3.55$, $\tan\delta = 0.0025$, and $\sigma_c = 5.8 \times 10^6$ S/m

2.3 Rat-Race Functioning Principle

The 180-hybrid, commonly referred to as rat-race, is a microwave network in which 4 ports are interconnected in a ring structure composed of three quarter-wavelength $\lambda/4$ sections and one three-quarter-wavelength $3\lambda/4$ section. A microstrip line implementation of this component is shown in **??**. Considering the ring with constant characteristic impedance and all the ports matched, at the central frequency, a signal applied to any port evenly splits and propagates along the clockwise (CW) and counterclockwise (CCW) directions. This equal power division is the result of the structure's symmetry, which ensures that the two propagation paths have the same impedance seen from the ports.

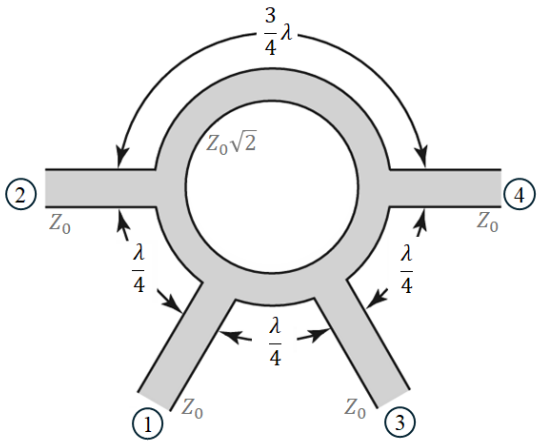

Figure 9: Rat-race coupler Structure

When port 1 is driven, the input splits in CW and CCW components, each reaching the output ports 2 and 3 with a phase shift of $\theta = \frac{360°}{\lambda} \cdot \frac{\lambda}{4} = 90°$ relative to the input. Port 4 acts as the isolated port, since it is reached by CW and CCW signals of equal amplitude but 180° phase difference, resulting in destructive interference and cancellation.

Conversely, if port 4 is driven, the CW signal propagates for $l = \lambda/4$, reaching port 3 with a $\theta = 90°$ phase shift, while the CCW signal travels for $l = 3\lambda/4$ arriving at port 2 with a $\theta = 270°$ phase shift. In this case, port 1 becomes the isolated port, and the two outputs on ports 2 and 3 exhibit a 180° phase difference.

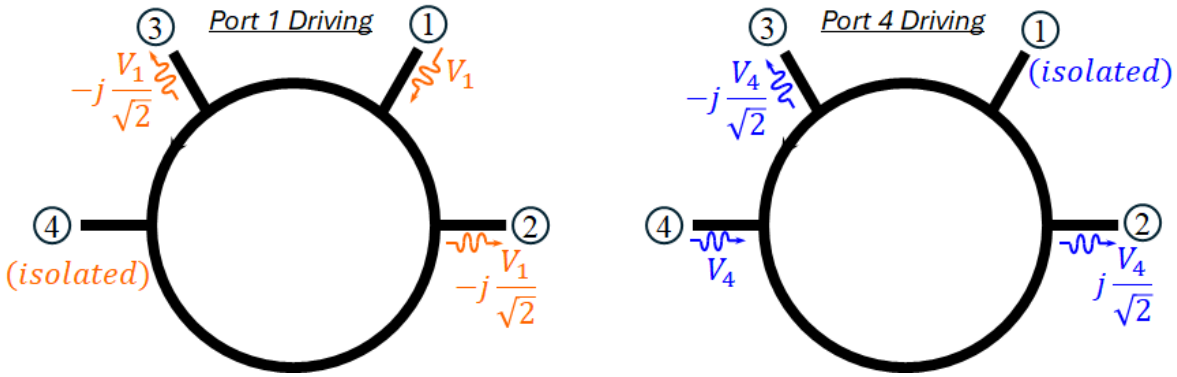

Figure 10: Rat-race coupler as power divider

A mirrored behavior is observed when ports 2 and 3 are excited. Specifically, when port 3 is excited, the power splits equally between ports 1 and 4, with the two outputs in phase, and

port 2 is isolated (mirroring the behavior when port 1 is driven). If port 2 is excited, the power again splits between port 1 and 4; however, now port 3 is isolated, and the outputs exhibit a 180° phase difference (mirroring the behavior when port 4 is driven).

The description so far refers to the rat-race used as a power divider. However, due to the reciprocity of the component, it can also operate as a power combiner/coupler, producing both the sum and the difference of the two inputs. When ports 1 and 4 are simultaneously excited, the signal on port 2 is the difference of the inputs, while the signal on port 3 is their sum, with ports 1 and 4 remaining isolated from each other. The same mirrored behavior occurs when port 2 and 3 are driven,

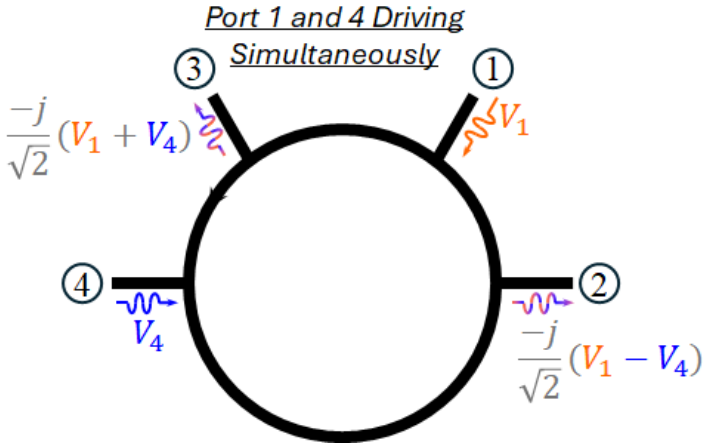

Figure 11: Rat-race coupler as power combiner

The S-matrix of the component is derived in Chapter 2.3 and the final result is shown in Equation 2.16.

$$[S] = \frac{-j}{\sqrt{2}} \begin{bmatrix} 0 & 1 & 1 & 0 \\ 1 & 0 & 0 & -1 \\ 1 & 0 & 0 & 1 \\ 0 & -1 & 1 & 0 \end{bmatrix} \tag{2.16}$$

The analysis of the 180-hybrid is conducted using the even and odd mode analysis technique, as described in [22], [33] and [37]. The aim is to derive the scattering matrix of the component in order to characterize its transmission properties and investigate the effect of the structural features on the device's behavior.

2.3.1 Even and Odd Mode Analysis of a 180-Hybrid Ring

The linearity of Maxwell equations solutions in microstrip lines, combined with the symmetry of the 180-hybrid along its vertical axis, enables the decomposition of any quasi-TEM excitations in the structure within two orthogonal quasi-TEM modes, namely the even and odd modes. The even mode exhibits a symmetric field distribution as generated by two inputs with identical amplitudes and phases applied on two symmetric ports. The consequence of these excitations is a zero current that crosses the vertical axis as if an open circuit is present. On the contrary, the odd mode presents an antisymmetric field distribution, as if the inputs on the two ports have the same amplitude but opposite phase. In this case, the current across the symmetry axis is maximized, as if a short circuit is present. According to these assump-

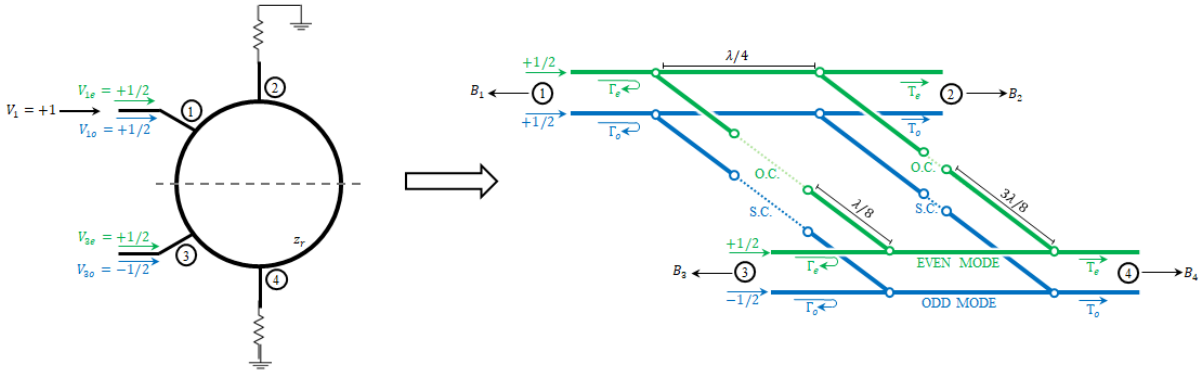

Figure 12: Even and Odd mode two-ports decomposition considering ports 1 excited by a unit incident wave .

tions, the four-port rat-race ring can be considered the superposition of two simplified two-port networks: one for the even mode and one for the odd mode.

Let us now consider the case of port 1 driven by a unit amplitude incident wave. As explained in the previous section, the input power is evenly divided, reaching ports 2 and 3 with the same phase, while port 4 remains isolated. This scenario can be modeled as the superposition of two simpler two-port networks receiving the excitations as in Figure 12. The overall scattered waves exiting from the rat race ports are then the combination of the reflections and transmission coefficients of the two-port networks as in Equation 2.17

$$
\begin{aligned}
B_1 &= \frac{1}{2}(\Gamma_e + \Gamma_o) \\
B_2 &= \frac{1}{2}(T_e + T_o) \\
B_3 &= \frac{1}{2}(\Gamma_e - \Gamma_o) \\
B_4 &= \frac{1}{2}(T_e - T_o)
\end{aligned}
\tag{2.17}
$$

The even and odd modes reflection and transmission coefficients are calculated considering the ABCD matrices of the even and odd mode two-port, that are in turn obtained as the product between the ABCD matrices of 3 sections in series: a $\lambda/8$ stub (open-circuited in even mode and short-circuited in odd mode), a $\lambda/4$ transmission line and a $3\lambda/8$ stub (likewise open circuited for the even mode and short-circuited for the odd mode). All these sections have the same characteristic impedance z_r normalized with respect to the port impedance Z_0. The evaluation of the ABCD matrices is presented in Figure 13.

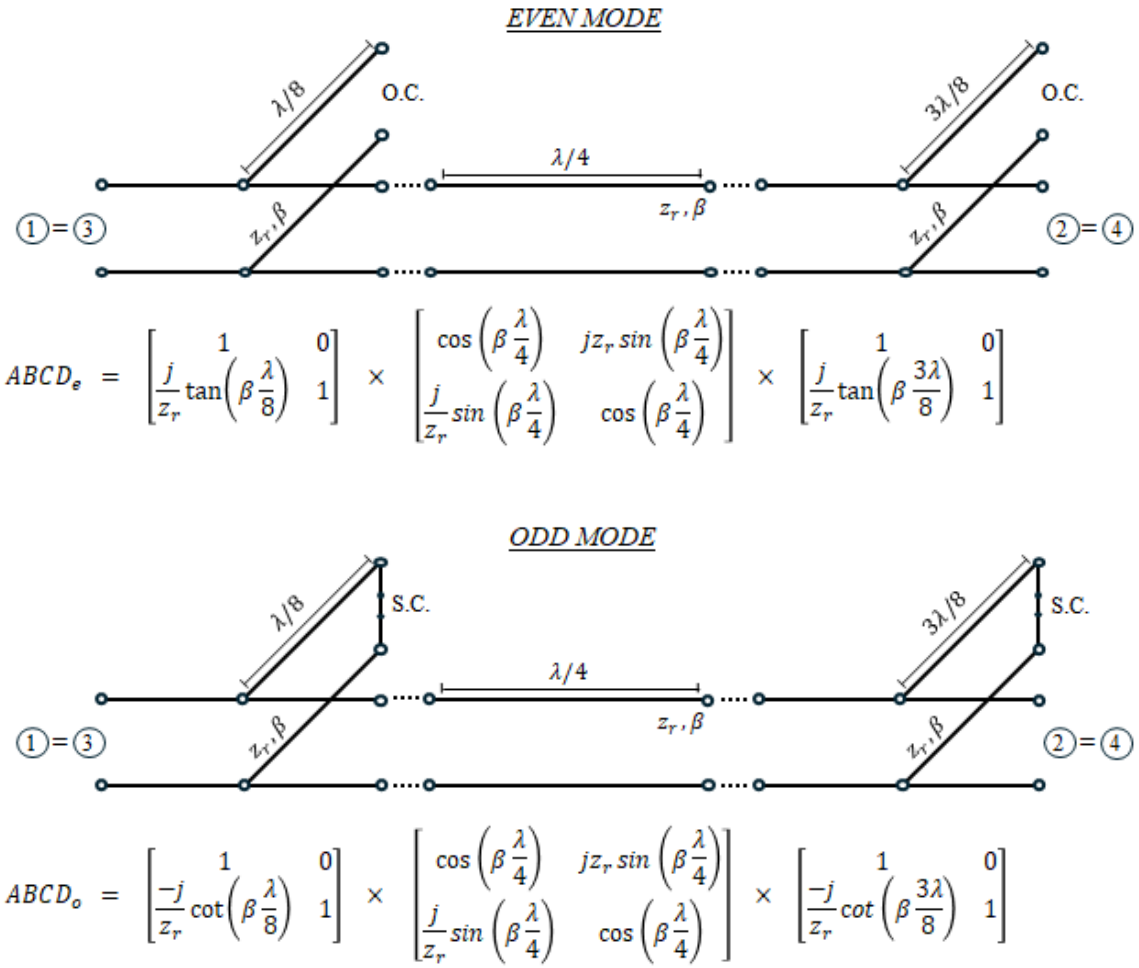

Figure 13: ABCD matrices for even and odd mode equivalent circuits of the rat-race hybrid.

At the central frequency, the matrices simplify as Equation 2.18.

$$ABCD_e = \begin{bmatrix} 1 & jz_r \\ \frac{2j}{z_r} & -1 \end{bmatrix} \qquad ABCD_o = \begin{bmatrix} -1 & jz_r \\ \frac{2j}{z_r} & 1 \end{bmatrix} \tag{2.18}$$

The reflection and transmission coefficients are now evaluated using the formulas in Equation 2.19 [22], obtaining the expressions in Equation 2.20.

$$\Gamma = \frac{A + B - C - D}{A + B + C + D} \qquad T = \frac{2(AD - BC)}{A + B + C + D} \tag{2.19}$$

$$\begin{aligned} \Gamma_e &= \frac{-2 + z_r(z_r - 2j)}{z_r^2 + 2} & \Gamma_o &= 1 + \frac{2j(z_r + 2j)}{z_r^2 + 2} \\ T_e &= -\frac{j2z_r}{z_r^2 + 2} & T_o &= -\frac{j2z_r}{z_r^2 + 2} \end{aligned} \tag{2.20}$$

Finally, substituting Equation 2.20 into Equation 2.17, the amplitude of the scattered waves exiting from the two ports are in Equation 2.21 [22].

$$\begin{aligned} B_1 &= s_{11} = 1 - \frac{4}{z_r^2 + 2} \\ B_2 &= s_{21} = -\frac{j2z_r}{2 + z_r^2} \\ B_3 &= s_{31} = -\frac{j2z_r}{2 + z_r^2} \\ B_4 &= s_{41} = 0 \end{aligned} \tag{2.21}$$

The expressions in Equation 2.21 also correspond to the first column of the scattering matrix.

Considering now the case of port 4 driven by a unit amplitude wave, the excitations on the ports are instead as in figure Figure 14, and the overall scattered waves are as in Equation 2.22 [22].

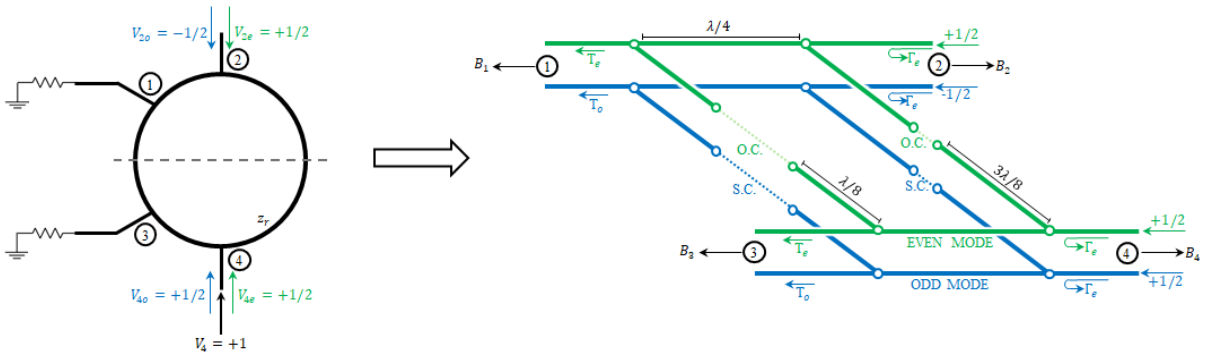

Figure 14: Even and odd mode decomposition when port 4 is driven by unit amplitude wave

$$
\begin{aligned}
B_1 &= \frac{1}{2}(T_e - T_o) \\
B_2 &= \frac{1}{2}(\Gamma_e - \Gamma_o) \\
B_3 &= \frac{1}{2}(T_e + T_o) \\
B_4 &= \frac{1}{2}(\Gamma_e + \Gamma_o)
\end{aligned}
\tag{2.22}
$$

Calculating again ABCD matrices of the two-ports networks for both the even and odd modes in Figure 14, then the Γ and T using Equation 2.19, the expressions for the scattered waves are the one in Equation 2.23

$$
\begin{aligned}
B_1 &= s_{14} = 0 \\
B_2 &= s_{24} = \frac{j2z_r}{2+z_r^2} \\
B_3 &= s_{34} = -\frac{j2z_r}{2+z_r^2} \\
B_4 &= s_{44} = 1 - \frac{4}{z_r^2+2}
\end{aligned}
\tag{2.23}
$$

Recalling that the behavior of the device when ports 2 and 3 are driven mirrors that observed when ports 4 and 1 are driven, respectively, the complete scattering matrix is composed as in Equation 2.24.

$$
[S] = \begin{bmatrix}
(1-\frac{4}{z_r^2+2}) & -\frac{j2z_r}{2+z_r^2} & -\frac{j2z_r}{2+z_r^2} & 0 \\
-\frac{j2z_r}{2+z_r^2} & (1-\frac{4}{z_r^2+2}) & 0 & \frac{j2z_r}{2+z_r^2} \\
-\frac{j2z_r}{2+z_r^2} & 0 & (1-\frac{4}{z_r^2+2}) & -\frac{j2z_r}{2+z_r^2} \\
0 & \frac{j2z_r}{2+z_r^2} & -\frac{j2z_r}{2+z_r^2} & (1-\frac{4}{z_r^2+2})
\end{bmatrix}
\xrightarrow{z_r=\sqrt{2}}
\frac{-j}{\sqrt{2}}
\begin{bmatrix}
0 & 1 & 1 & 0 \\
1 & 0 & 0 & -1 \\
1 & 0 & 0 & 1 \\
0 & -1 & 1 & 0
\end{bmatrix}
\tag{2.24}
$$

The overall scattering matrix shows that, at the central frequency, the characteristic impedance of the ring z_r has no influence on the isolation and on the division ratio between the outputs, which always remains equal split. The matching of the ports is instead dependent on z_r and the condition of no power reflected is obtained for $z_r = \sqrt{2}$, when both outputs receive the 50% of all available input power.

2.3.2 Frequency Behavior of the component

The analysis in the previous section was conducted considering the component at the design frequency. The aim of this section is instead to show the component behavior when the frequency varies.

Let us consider again the case of port 1 to be driven. Recalling Figure 13, the ABCD matrices are functions of $\tan(\beta l)$, $\cos(\beta l)$ and $\sin(\beta l)$, where l is the line length and $\beta = 2\pi/\lambda$ is the propagation constant. Considering $\tan(\beta\ \lambda/8) = \tan(\theta) = t$, we can express these functions as in Equation 2.25 using trigonometric identities.

$$\cos\left(\beta\,\frac{\lambda}{4}\right) = \frac{1-t^2}{1+t^2} \qquad \sin\left(\beta\,\frac{\lambda}{4}\right) = \frac{2t}{1+t^2} \qquad \tan\left(\beta\,\frac{3\lambda}{4}\right) = \frac{3t-t^3}{1-3t^2} \tag{2.25}$$

Substituting Equation 2.25 into the equations in Figure 13, we obtain Equation 2.26, which are the analytic expressions of the even and odd ABCD matrices as functions the frequency through t.

$$\begin{aligned} ABCD_e &= \begin{bmatrix} -\dfrac{5t^4-10t^2+1}{3t^4+2t^2-1} & \dfrac{j2z_r\,t}{t^2+1} \\ -\dfrac{2j\,t(t^2-3)}{z_r(t^2+1)} & -\dfrac{3t^2-1}{t^2+1} \end{bmatrix} \\ ABCDo &= \begin{bmatrix} \dfrac{t^4-10t^2+5}{-t^4+2t^2+3} & \dfrac{j\,2\sqrt{2}\,t}{t^2+1} \\ \dfrac{j\,\sqrt{2}\,(3t^2-1)}{t^3+t} & -\dfrac{t^2-3}{t^2+1} \end{bmatrix} \end{aligned} \tag{2.26}$$

The total scattering matrix is finally obtained by repeating the steps in Chapter 2.3.

The amplitudes of the scattering parameters, when the device operates as a power divider driven by port 1 or port 4 are shown in Figure 15 and Figure 15. These plots are obtained from Equation 2.26 substituting the propagation constant in of $t = \tan\left(\beta \frac{\lambda}{8}\right)$ with

$$\beta = \frac{2\pi}{\lambda} = \frac{2\pi f}{c_0}\sqrt{\epsilon_{eff}} \tag{2.27}$$

where $\epsilon_{eff} = 2.66$, $c_0 = 3 \cdot 10^8$ m/s and f ranging from 1 GHz to 10 GHz.

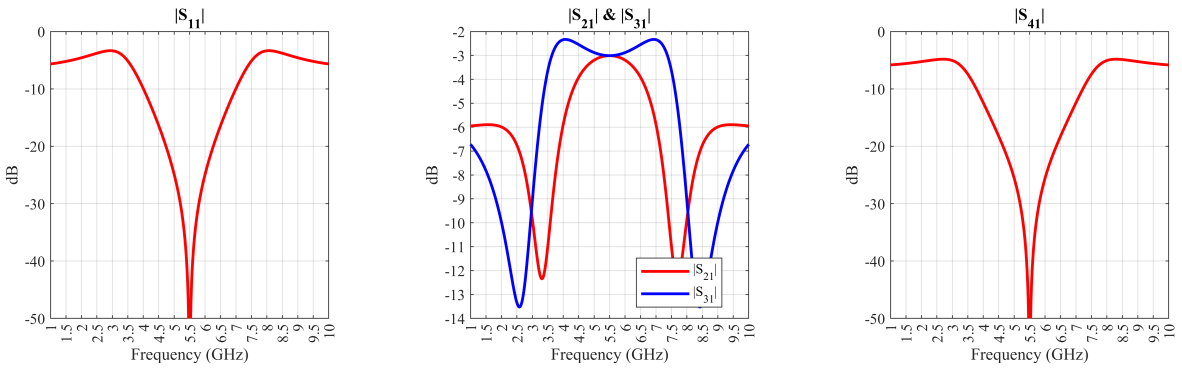

(a) **(b)** **(c)**

Figure 15: Plot of scattering parameters amplitude considering port 1 driving, $\epsilon_r = 3.55$, $\epsilon_{eff} = 2.66$ and central frequency $f_0 = 5.5\,GHz$

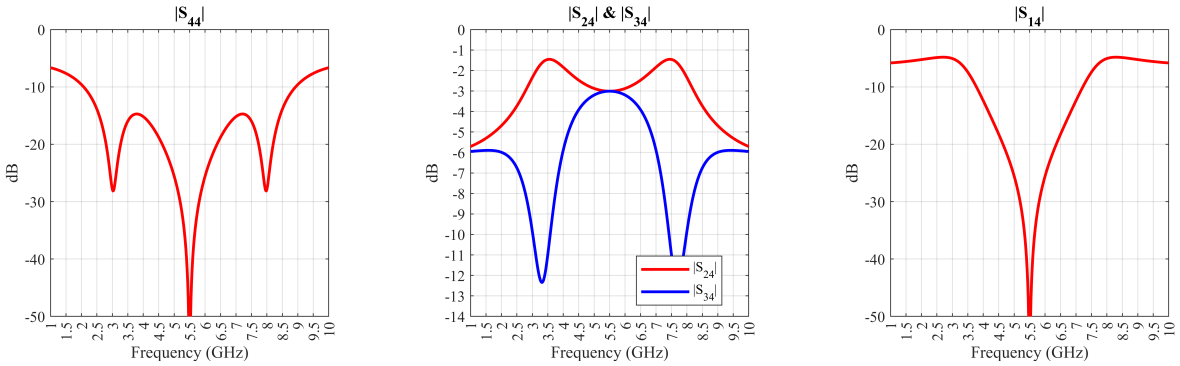

(a) **(b)** **(c)**

Figure 16: Plot of scattering parameters amplitude considering port 4 driving, $\epsilon_r = 3.55$, $\epsilon_{eff} = 2.66$ and central frequency $f_0 = 5.5\,GHz$

The phase difference between the two outputs is illustrated in Figure 17 (a) when port 1 is driving and in Figure 17(b) when port 4 is driving.

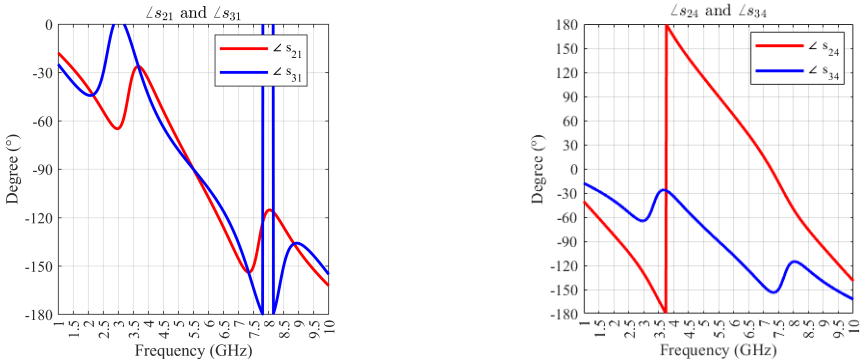

(a) **(b)**

Figure 17: Plot of the phase of the outputs in a rat-race ring with $\epsilon_r = 3.55$, $\epsilon_{eff} = 2.66$ and central frequency $f_0 = 5.5\,GHz$

2.4 Performance of the Ideal 180-Hybrid Ring and Metrics

Observing Figure 15, Figure 16 and Figure 17, the ideal rat-race has port matching with $|s_{11}|$ below -20dB between 4.75 GHz and 6.25 GHz, and $|s_{44}|$ below -20dB between 4.6 GHz and 6.4 GHz. The isolation level $|s_{41}|$ and $|s_{14}|$ are below -30dB in a 500 MHz band between 5.25 GHz and 5.75 GHz. while, considering the output power splitting, we have that $|s_{24}|$, $|s_{34}|$, $|s_{21}|$ and $|s_{31}|$ remain in the range of -3 dB around the design frequency.

To evaluate the performances of the device as a coupler, we consider the magnitude imbalance and the phase imbalance on the two outputs as metrics. The magnitude imbalance is the absolute difference between the magnitudes of s_{21} and s_{24} for the difference port 2, and between the magnitudes of s_{31} and s_{34} for the sum port 3. This should remain within ± 0.5 dB for the

performances to be acceptable. The phase imbalance is instead the absolute difference between the phases of the signals that reach ports 2 and 3. In the case of the difference port 2, this is the difference between $\angle s_{21}$ and $\angle s_{24}$, and is expected to remain within $\pm 10°$ around $180°$ in the operative frequency range. In the case of the sum port 3, this is the difference between $\angle s_{31}$ and $\angle s_{34}$ and is expected to remain within $\pm 10°$ in the operative frequency range.

The phase and amplitude imbalance of the ideal rat-race are shown in Figure 18.

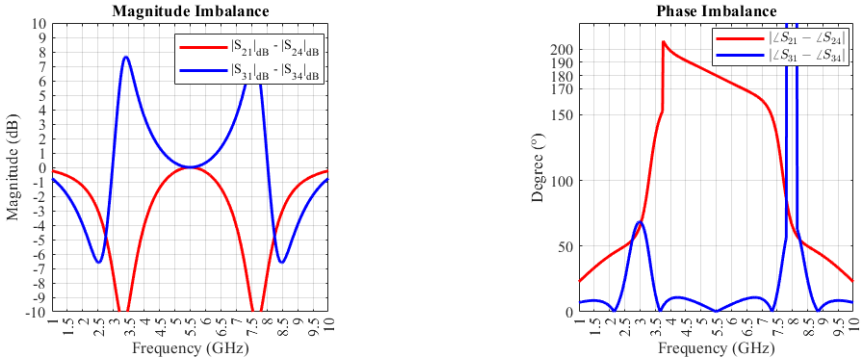

(a) **(b)**

Figure 18: Plot of the amplitude and phase imbalance in a rat-race ring with $\epsilon_r = 3.55$, $\epsilon_{eff} = 2.66$ and central frequency $f_0 = 5.5\,GHz$

2.5 CAD Tools and Simulation Environment

In modern RF circuit design, the CAD tool has become essential to obtain a reliable understanding of the component performance before the physical fabrication. The analytical models are often based on complex approximations that fail to capture real-world behaviors, which can significantly affect component behavior.

In this work, Keysight Advanced Design System (ADS) has been employed as the primary environment for the design, simulation, and optimization of the rat-race ring. This enabled precise tailoring of the component's behavior for Self-Interference Cancellation in IBFD systems.

Keysight ADS is a leading Electronic Design Automation (EDA) software used in both industry and academia for RF and microwave circuit design. It unifies the schematic design, circuit simulation, layout generation, and electromagnetic analysis in the same environment, allowing the modeling of both the ideal transmission line behavior in the initial design and the real-world parasitic effects in the EM analysis.

The design workflow starts with the implementation of the component using ideal transmission line elements in the schematic, for a rapid validation of the theoretical behavior and focus on key performances across the frequency band, as isolation. The transition from the ideal model to a realizable component follows with the implementation of microstrip elements in the schematic. In this stage, the built-in LineCal tool is used to calculate the microstrip's physical length and width of the microstrip elements based on the substrate characteristics. At this point, particular attention is given to the bends and junctions that are necessary for the physical realization of the component, as these insert parasitic susceptances and admittances.

To mitigate these effects, which are neglected in the ideal theoretical modeling, multiple optimization iterations are conducted on the physical parameters of the microstrip . Following the microstrip schematic implementation, the circuit is translated into a physical layout using ADS Layout Editor, and EM simulations are performed to capture parasitic coupling, radiation losses, and discontinuity losses.

The EM simulations are conducted using Momentum Solver integrated in ADS, which aim to solve Maxwell's equations on the layout geometry to evaluate the electric and magnetic field distribution on the component. This provides insights into how the component will behave in the real world. It is also possible to conduct layout optimization with this simulation, although, due to the long time required, these are optimizations are tipically used for final fine-tuning of the component. By contrast, schematic simulations are much faster since they are based on idealized components represented with simplified models that do not account for many real-world effects. These are circuit-level simulation that relies on network analysis and aim to simulate the voltage, current, and power at different points of the circuit. Both these simulations types provide the network parameters of the component, typically the S-parameter, which are then exported and processed in other software, such as MATLAB, if post-processing is needed.

Once satisfied with the EM results, the layout of the component is exported in a usable format for fabrication.

The of advantages Keysight ADS as design and simulation platform are numerous. The integration between schematic and EM simulations in a single platform enables iteration between

schematic and layout without changing environments, so reducing design time. In addition, ADS offers a powerful optimization tool that automatically adjusts component parameters to meet performance goals, allowing for a tuning that would be too complex if based on theoretical models only. Finally, the Momentum EM solver provides results that closely match those of the real component, giving high degree of confidence in the performance expected by the fabricated component. The main drawback is the computational complexity required by the full-wave EM simulation, especially when using fine meshes or when simulating large components. EM simulation requires significant processing power and simulation time, especially if high resolution and a broad frequency range coverage are needed.

In conclusion, Keysight ADS is a powerful and versatile CAD tool that has been very helpful to validate the theory, design, optimize and simulate the rat-race ring in this work.

CHAPTER 3

DESIGN OF A WIDEBAND HIGH-ISOLATION RAT-RACE COUPLER

In Chapter 2.3, it has been demonstrated that the conditions of input matching and maximum power transmitted to the outputs are obtained when the characteristic impedance of the ring is $Z_r = Z_0\sqrt{2}$, where Z_0 is the ports impedance. However, in real-world implementations of the component, such as the one in microstrip proposed in this thesis, the characteristic impedance of a line is a function of the frequency. Consequently, the optimal matching condition mentioned before can be obtained at the design frequency only, and the device is inherently narrowband. To achieve the goal of a wideband rat-race ring, it is necessary to minimize the variation of the impedances in the ring over a wide frequency band.

3.0.1 Effect of multi-section transformers in ring branches

Let us consider the half-symmetrical section of the component as illustrated in Figure 19. In the first part of this chapter we are going to analyze the rat-race to calculate the impedances Z_{in_1} and Z_{in_2} shown in Figure 19.

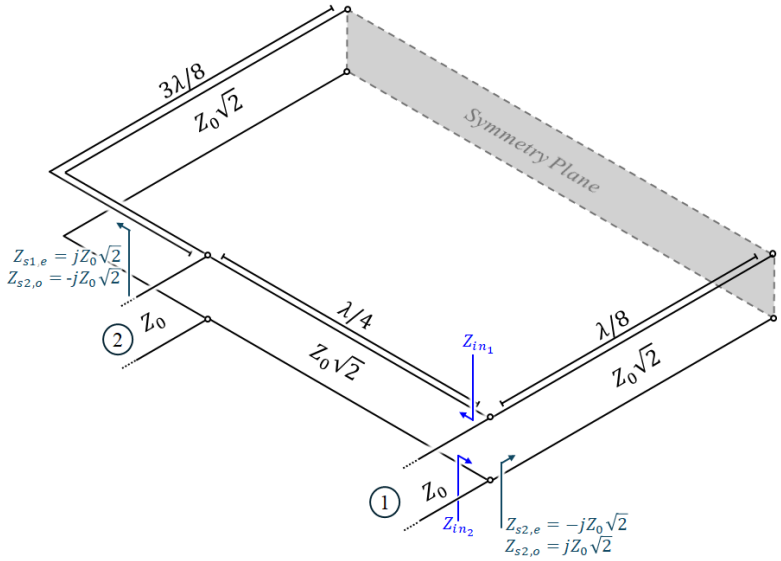

Figure 19: Section of narrowband rat-race coupler

Z_{in_1} is the input impedance of the $\lambda/4$ section that is loaded with the parallel combination of the port 2 termination (Z_0) and the input impedance of the $3\lambda/8$ stub, which is, in turn, open-circuited in the even-mode analysis $\left(Z_{s1,e} = jZ_0\sqrt{2}\right)$ and short-circuited in the odd-mode $\left(Z_{s1,o} = -jZ_0\sqrt{2}\right)$. With this considerations, $Z_{in_{1,e}}$ and $Z_{in_{1,o}}$ are calculated as in Equation 3.1

$$Z_{in_{1,e}} = \frac{\left(Z0 \parallel jZ_0\sqrt{2}\right)^2}{Z_0\sqrt{2}} \qquad Z_{in_{1,o}} = \frac{\left(Z0 \parallel -jZ_0\sqrt{2}\right)^2}{Z_0\sqrt{2}} \tag{3.1}$$

Assuming the case of port 1 driving the component, the total voltage on Z_{in_1} can be expressed as in Equation 3.2.

$$
\begin{aligned}
V_1 &= V_{1,e} + V_{1,o} = 2\,V_{1,e} \\
I_{Z_{in_1}} &= I_{Z_1,e} + I_{Z_1,o} = \frac{V_{1,e}}{Z_{in_{1,e}}} + \frac{V_{1,o}}{Z_{in_{1,o}}} = V_{1,e}\left(\frac{Z_{in_{1,e}} + Z_{in_{1,o}}}{Z_{in_{1,e}} Z_{in_{1,o}}}\right)
\end{aligned}
\tag{3.2}
$$

Combining Equation 3.1 and Equation 3.2, the total $Z_{in_{1,e}}$ can be evaluated as in Equation 3.3.

$$
Z_{in_1} = \frac{V_1}{I_{Z1}} = \frac{2\,Z_{in_{1,e}} Z_{in_{1,o}}}{Z_{in_{1,e}} + Z_{in_{1,o}}} = 2\left(Z_{in_{1,e}} \parallel Z_{in_{1,o}}\right) = Z_0\sqrt{2} \tag{3.3}
$$

Z_{in_2} is instead the parallel between the port 1 termination (Z_0) and the $\lambda/8$ stub, which open circuited in even-mode $\left(Z_{s2,e} = -jZ_0\sqrt{2}\right)$ and short-circuited in odd-mode $\left(Z_{s2,e} = jZ_0\sqrt{2}\right)$. The voltage on Z_{in_2} is still $V_1 = V_{1,e} + V_{1,o} = 2\,V_{1,e}$, so the total impedance Z_{in_2} are calculated in Equation 3.5, with the same procedure as Equation 3.2 and Equation 3.3

$$
Z_{in_{2,e}} = \left(Z0 \parallel -jZ_0\sqrt{2}\right) \qquad\qquad Z_{in_{2,o}} = \left(Z0 \parallel jZ_0\sqrt{2}\right) \tag{3.4}
$$

$$
Z_{in_2} = 2\left(Z_{in_{2,e}} \parallel Z_{in_{2,o}}\right) = Z_0 \tag{3.5}
$$

The high symmetry of the components ensures that at design frequency this same impedance set is seen at driving port junction when any other port is driven.

To minimize the frequency dependent variations of Z_{in_1} and Z_{in_2} over a broader range, this thesis proposes the the novel solution of implementating the symmetrical Chebyshev multi-section transformer illustrated in Figure 20 between port 1 and 2, and between port 3 and

4 (to maintain the symmetry along the vertical axis). This implementation ensures that the impedance seen through the $\lambda/4$ branch remains close to its design value of $Z_{in_1} = Z_0\sqrt{2}$ over a wider frequency band. In addition, due to the symmetry of the transformer itself, this improvement in bandwidth holds regardless of which port is driven.

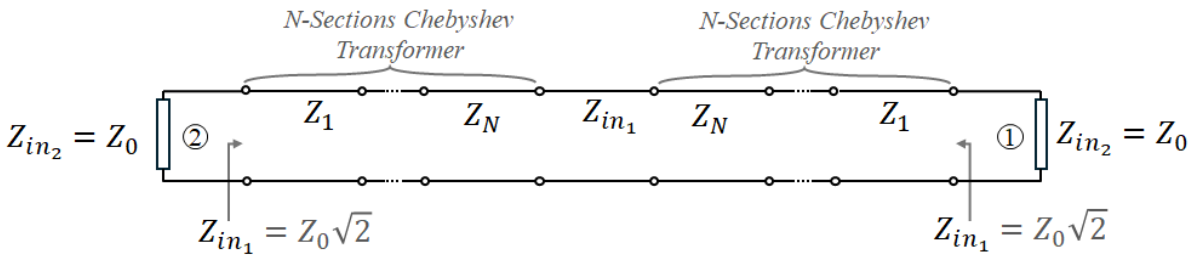

Figure 20: Symmetric multisection transformer implemented in between port 1 and 2 (identical for in between port 3 and 4 due to symmetry)

When port 1 is driven, the signal is expected to split evenly between ports 2 and 3, propagating on two identical electrical paths. For this reason, the same multi-section structure implemented between ports 1 and 2 has to be implemented also between ports 1 and 3.

In addition, the expressions presented in Equation 2.20 show that the isolation of port 4 primarily relies on the 270° phase shift introduced by the transmission line rather than on the impedance matching. Since multi-section transformers have a negligible effect on the phase and do not produce any significant smoothing on the phase variation, implementing the same

structure between ports 2 and 4 would offer minimal benefits if compared with the increase in design complexity. For this reason, multisection structures are not implemented in between ports 2 and 4,

To meet the requirement of an overall transformer length of $\lambda/4$ (to fit in the branches), the number of sections has to be carefully selected to optimize the matching performances. The transformer is designed to simultaneously match both ports to the impedance Z_{in_2}, so the transformer can be considered the union of two multi-section transformers, each matching one of the connected ports. While increasing the number of sections enhances matching capability, it also reduces the electrical length of each section to maintain the overall transformer length at $\lambda/4$. However, as shown in the previous chapter, shorter sections negatively impact the matching capabilities of the transformer. A good trade-off between section numbers and length is found with a total of 9 sections, each with an electrical length of $10°$, ensuring both the compactness of the design and noticeable improvements in the component bandwidth. An illustration of the proposed structure is provided in Figure 21.

Among the different profiles analyzed earlier for the multisection transformers, the Klopfenstein taper ensures the best performance for the reduced length of the transformer. However, since this component must be fabricated using a CNC machine, the tight manufacturing process tolerances make the Klopfenstein profile unsuitable and move the choice to the Chebyshev profile to maximize the bandwidth.

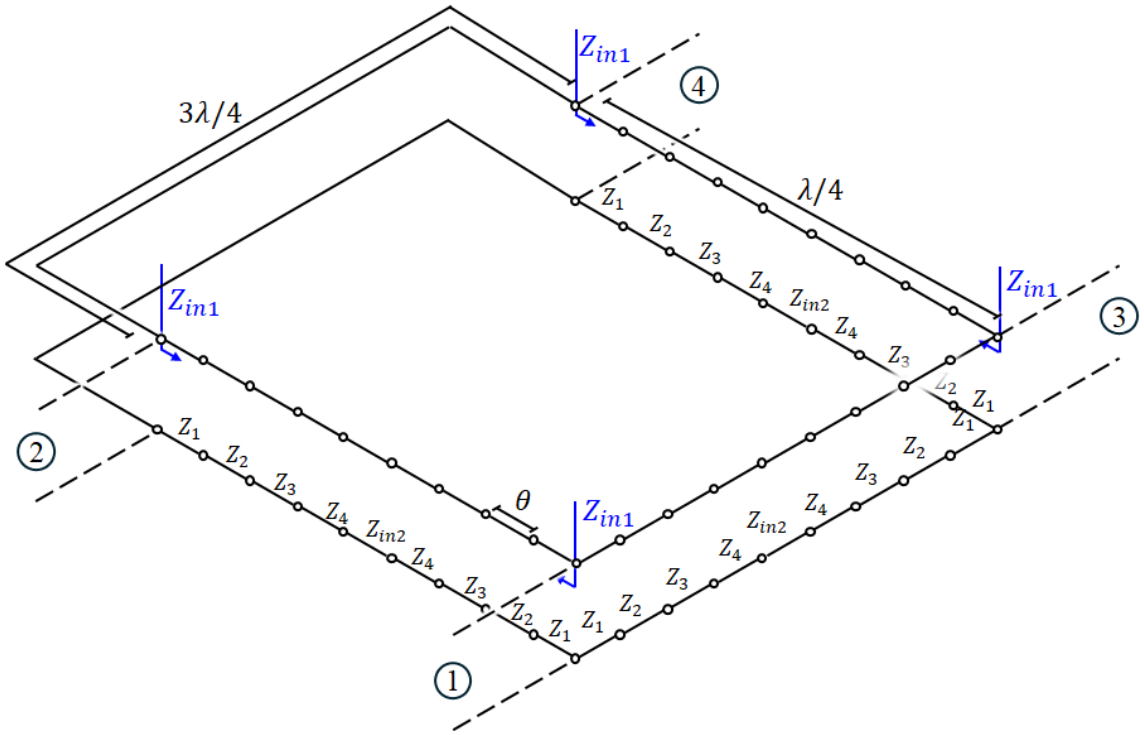

Figure 21: Illustration of the proposed rat-race structure with multisection transformers

The structure in Figure 21 has been simulated in Keysight ADS using ideal transmission lines and center frequency of $f_c = 5.5$ GHz. Figure 22 compares the performance of the proposed configuration with the ideal rat-race ring presented in Chapter 2.3.

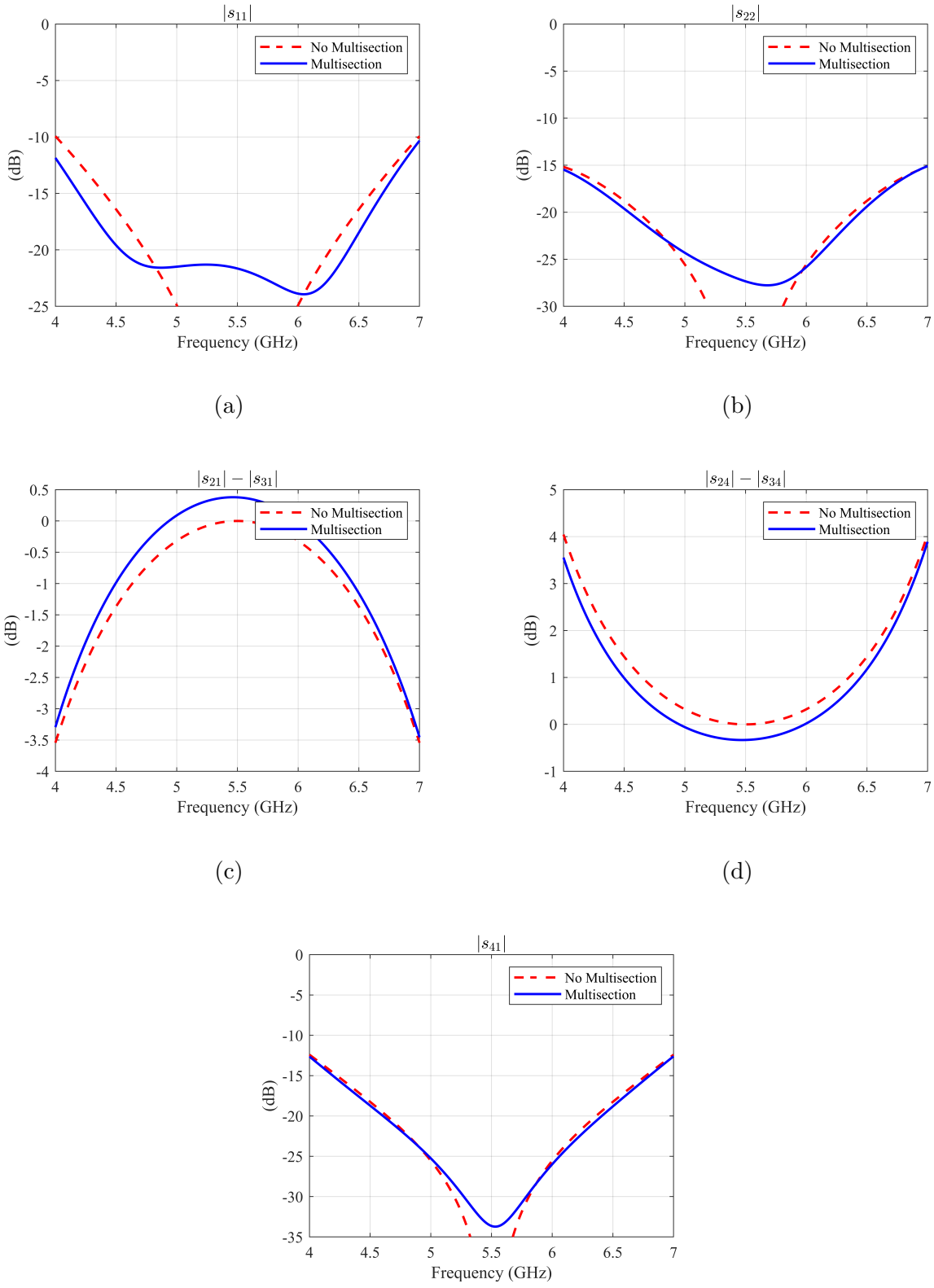

Figure 22: Convetional and improved structure performances.

As shown in Figure 22(a), the structure with multi-section transformer exhibits improved matching on port 1, with s_{11} remaining below 20dB across the frequency range from 4.5 GHz and 6.4 GHz. This represents an improvement of the bandwidth improvement of 350 MHz, corresponding to a 25% compared to the conventional structure

Considering instead the amplitude imbalance, Figure 22(c) and Figure 22(d) show a 30% increase in the frequency range in which the phase imbalance remains in the acceptable range for both port 1 or port 4 driving. By contrast, the improvements in isolation and port 2 matching are modest. The -20dB bandwidth of $|s_{22}|$ increases by approximately 10%, while the corresponding improvement for $|s_{41}|$ is limited to 4%.

As observed in Figure 22 (a) and (b), implementing multisection transformers results in an increase in the minimum matching level. This behavior can be attributed to Fano's limit discussed in Chapter 2.1.4, which imposes a trade-off between bandwidth and matching performance. Nevertheless, this phenomenon contributes to a flatter in-band response, which is advantageous for systems operating over a wide frequency range, such as in-band full-duplex systems, since it ensures consistent performances across the entire operative range.

3.0.2 Effect of multi-section transformer for input port matching

The aim of this section is to present the additional novelty introduced in the proposed structure, which consists of the implementation of multi-section transformers in the branches connecting the ports to the ring. This results in an improvement of the isolation level and bandwidth, which are essential parameters for SIC in IBFD systems.

The first part provides an intuitive explanation of how these multi-section transformers affect isolation performance; the second part evaluates the isolation improvement obtained through their implementation.

Recalling the functioning principle of the rat-race described in Chapter 2.3, the isolation of the component relies on precise phase and amplitude relationships that are valid only at the central frequency for the CW and CCW signals that propagate in the ring.

At the central frequency, the branches that connect port 1 to 2, port 1 to 3, and port 3 to 4 exhibit an electrical length of $\theta = 90°$, while the branch that connects port 2 to 4 has an electrical length of $\theta = 270°$. This configuration ensures that, when port 1 is driven, the impedance seen along the CW and CCW paths is identical, resulting in an even -3 dB power split between them. As a consequence, port 4 is isolated as it is reached by signals with equal amplitude and a 180° phase shift that cancels each other. In this condition, any reflected wave that is re-injected in the ring through the ports interferes destructively on port 4, resulting in peak isolation performances.

As the frequency varies from the design value, the electrical length and the impedance of the branches vary, resulting in an uneven power split between the CW and CCW paths, a phase

deviation from 180° on port 4, and finally a deterioration of the isolation. The mismatch also increases, causing an increase in the reflections that do not cancel on port 4.

In this context, the insertion of multi-section transformers between the ring and the ports mitigates these effects by minimizing reflections on the ports and keeping the impedance seen toward the ports around Z_0 over a wider range. This latter effect, combined with the multisection transformers implemented in the branches, minimizes the impedance variation between the CW and CCW paths, resulting in an even power split maintained over a wider frequency band. In general, the combination of multisection transformers implemented in the branches and on the ports helps maintain the design impedance relationships over a wider range, significantly improving the isolation performance of the device.

Figure 23 compares isolation performances between the microstrip structure with and without the multisection transformers on the ports. The isolation level remains below −30 dB between 5 GHz and 6 GHz with an increase of 100% with respect to the structure with no multisection transformer implemented on the ports.

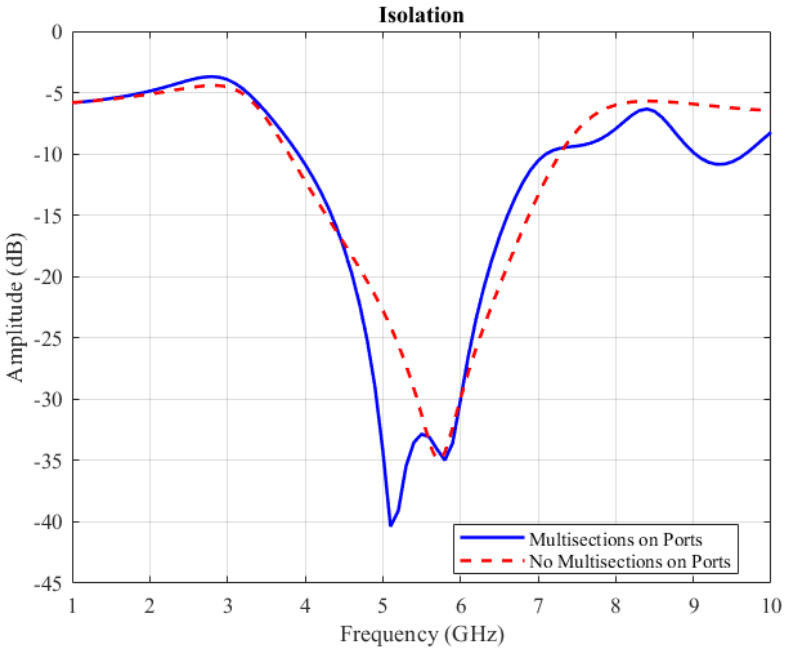

Figure 23: Illustration of ports 2 and 3 mismatch on isolation

3.1 Microstrip implementation

The structure discussed in the previous sections has been implemented using microstrip lines in Keysight Advanced Design System (ADS). The multisection structures were realized in microstrip lines on a RO4003C substrate, characterized by relative permittivity of $\epsilon_r = 3.55$, dielectric thickness of $h = 32$ **mil** (0.813 mm and loss tangent of $\tan\delta = 0.0025$. Based on these substrate's parameters, the width and length of the microstrip lines were evaluated using the formulas in Chapter 2.2, alternatively, through the LineCalc tool available in ADS for higher accuracy. Once the schematic with the microstrip lines was completed, it was optimized and simulated to assess the expected electrical performances

The physical layout of the component was then generated in ADS Layout Editor. In order to obtain results as close as possible to the fabricated device the circuit simulation performed on the schematic is not enough, so an electromagnetic simulation has been carried out on the layout mesh using Momentum Microwave, the full-wave solver available in ADS. Both a circular and a rectangular layout of the component has been generated and optimized. The rectangular layout is shown in Figure 24 with the key dimensions in Table III and the EM simulation results in Figure 25, the circular layout is instead shown in Figure 26 with the key dimensions in Table IV and the EM results in Figure 27.

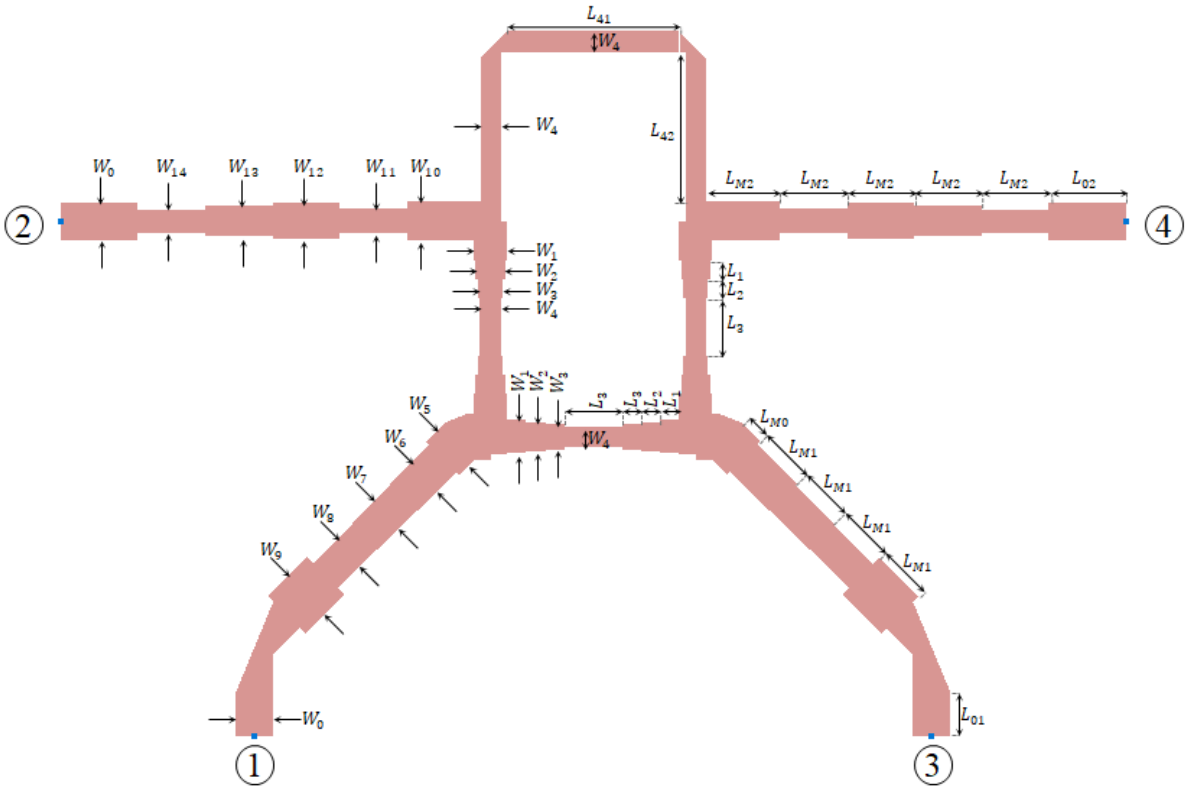

Figure 24: Rectangular Layout of the Proposed Microstrip Rat-Race Coupler

TABLE III: KEY DIMENSIONS OF THE RECTANGULAR LAYOUT

W_0	1.8 mm	L_1	0.92 mm	W_5	2.26 mm	W_{10}	1.83 mm	L_{M0}	1.0 mm
W_1	1.6 mm	L_2	0.92 mm	W_6	2.00 mm	W_{11}	1.27 mm	L_{M1}	2.65 mm
W_2	1.4 mm	L_3	1.84 mm	W_7	1.87 mm	W_{12}	1.76 mm	L_{M2}	3.24 mm
W_3	1.2 mm	L_{41}	8.28 mm	W_8	1.62 mm	W_{13}	1.50 mm	L_{01}	2.0 mm
W_4	1.0 mm	L_{42}	15.16 mm	W_9	2.41 mm	W_{14}	1.16 mm	L_{02}	3.72 mm

Observing the results of the rectangular layout in Figure 25, the most impressive improvement is in the isolation (Figure 25b) with both an increase in bandwidth and a decrease of more than -5dB in the average in-band isolation level. In detail, the amplitude of s_{41} remains below -25dB between 4.8GHz and 6.13GHz (BW = 1.33 GHz), and below -30dB between 4.9GHz and 6.0GHz (BW = 1.1 GHz). The reflection coefficients in Figure 25(a) increased in flatness and minimum amplitude value, with the -20 dB band between 4.5GHz and 6.63GHz (BW = 1.8 GHz) for s_{11} and between 2.7GHz and 6.4GHz (BW = 1.8 GHz) for s_{22}. In both port 2 and 3, the amplitude imbalance (Figure 25e) remains in the acceptable range of ± 0.5 dB between 4.25 GHz and 6.7 GHz (BW = 2.45 GHz), and also the phase imbalance (Figure 25f) remains in the acceptable range of $\pm 10^{\circ}$ also in this same range.

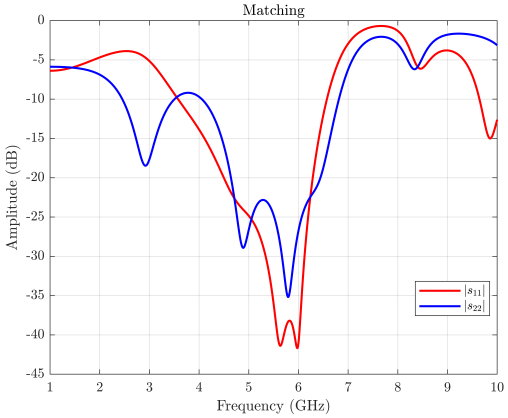

(a)

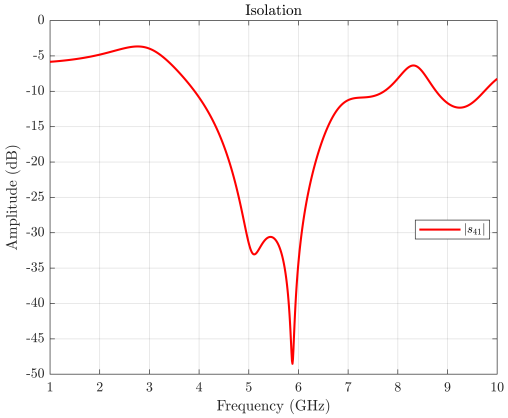

(b)

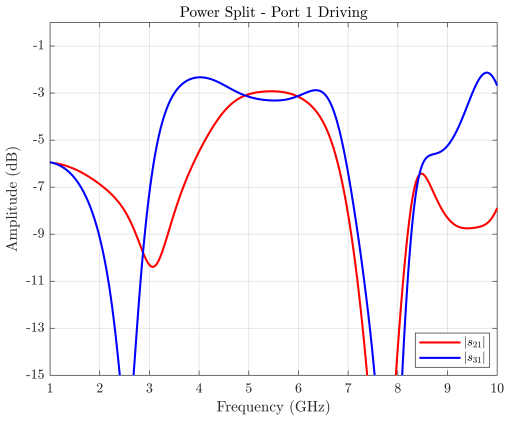

(c)

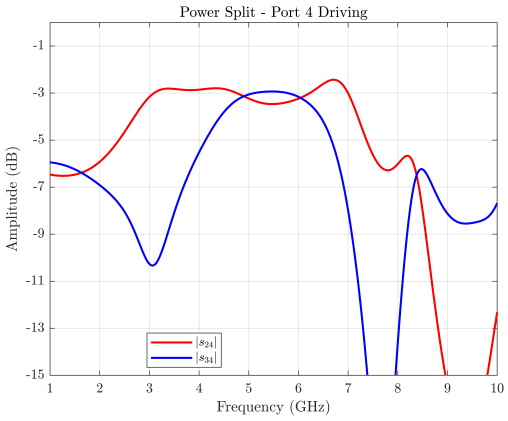

(d)

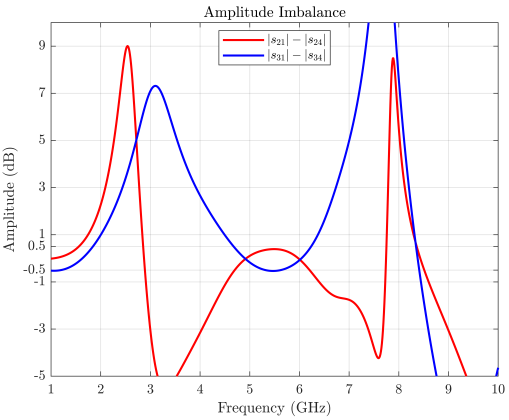

(e)

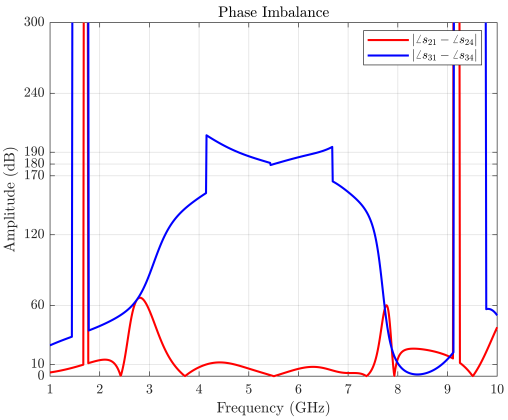

(f)

Figure 25: EM Simulation results of the microstrip rectangular rat-race coupler

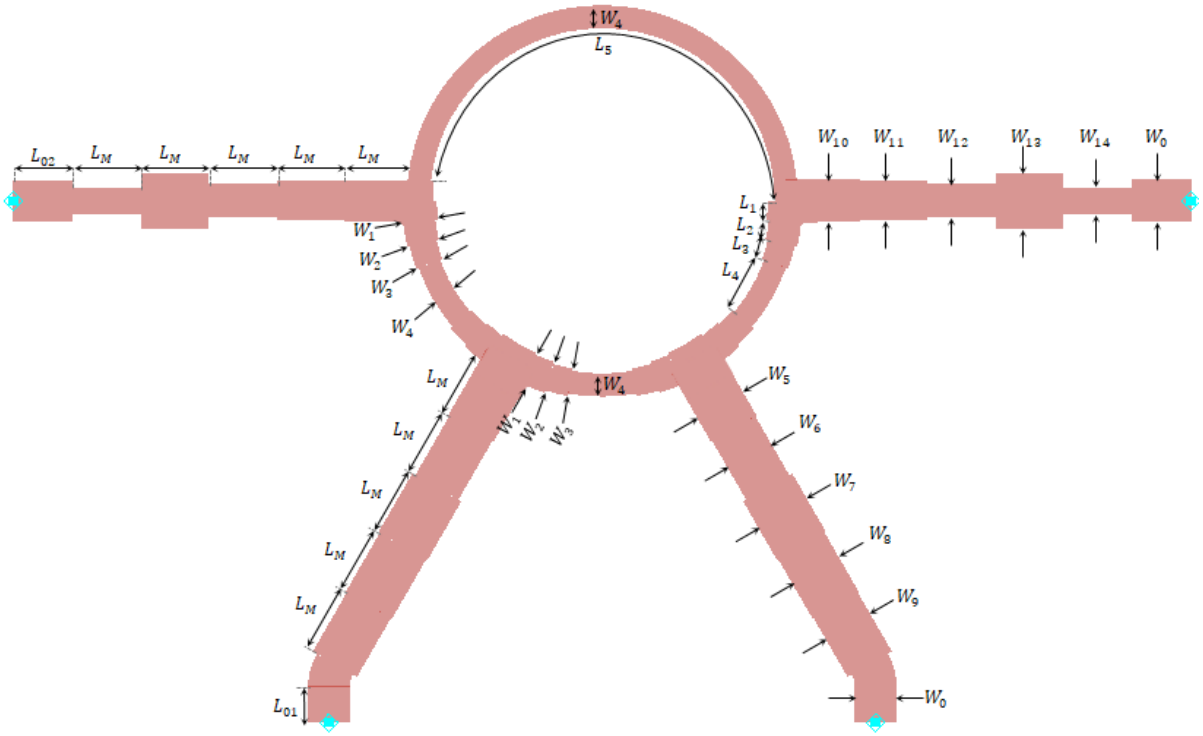

Figure 26: Circular Layout of the Proposed Microstrip Rat-Race Coupler

TABLE IV: KEY DIMENSIONS OF THE CIRCULAR LAYOUT

W_0	1.8 mm	L_1	1.39 mm	W_5	2.26 mm	W_{10}	1.81 mm	L_M	2.93 mm
W_1	1.6 mm	L_2	1.39 mm	W_6	2.14 mm	W_{11}	1.68 mm	L_{01}	3.39 mm
W_2	1.4 mm	L_3	1.39 mm	W_7	2.44 mm	W_{12}	1.43 mm	L_{02}	3.15 mm
W_3	1.2 mm	L_4	2.78 mm	W_8	2.31 mm	W_{13}	2.40 mm		
W_4	1.0 mm	L_5	37.41 mm	W_9	2.20 mm	W_{14}	1.12 mm		

With respect to the rectangular layout, the circular layout required much less optimization due to the absence of corners, however the manufacturing is more complex if cartesian CNC are involved. The results of the EM simulations on this layout ara shown in Figure 27 and appears very similar to the ones of the rectangular layout in Figure 24. The amplitude of s_{11} remains below -20 dB in a 1.8 GHz band between 4.7 GHz and 6.5 GHz, while s_{22} remain in the -20 dB band within 4.5 GHz and 6.4 GHz. The isolation performance slightly improved if compared to Figure 25, with s_{41} below -30 dB in the frequency range from 4.9 GHz and 6.3 GHz (BW = 1.4 GHz).

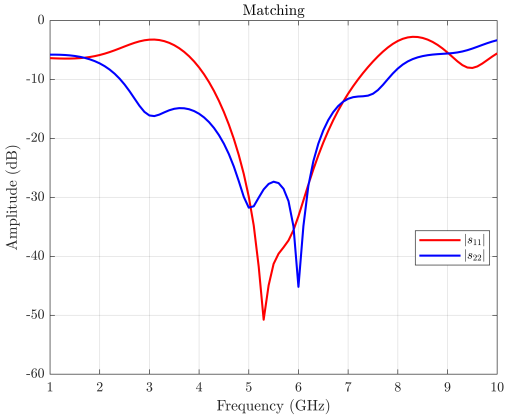

(a)

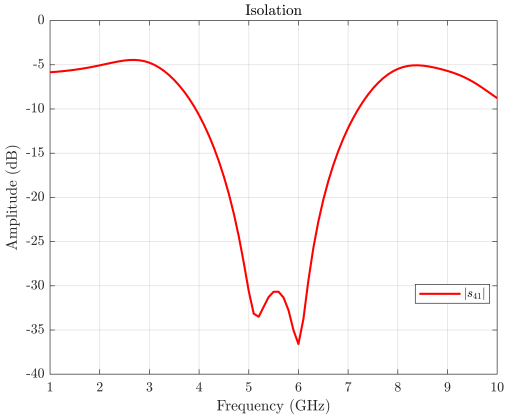

(b)

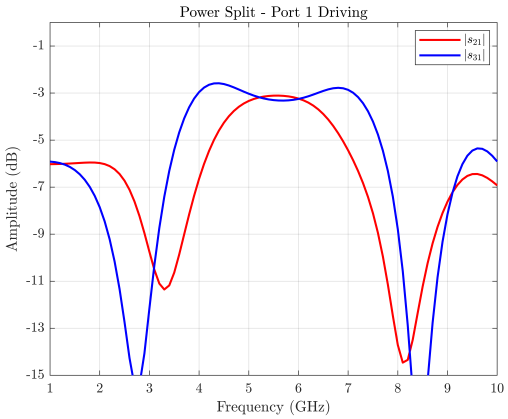

(c)

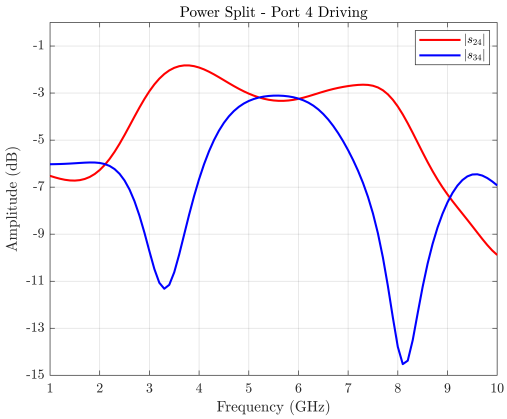

(d)

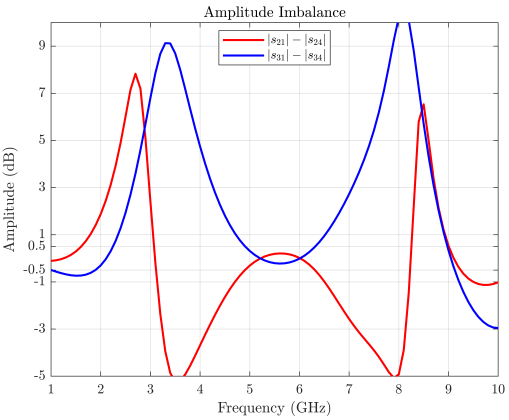

(e)

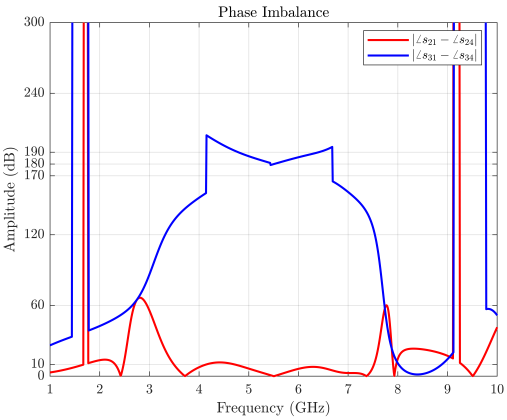

(f)

Figure 27: EM Simulation results of the microstrip Circular rat-race coupler

CHAPTER 4

CONCLUSION

4.1 Fabrication and Measurement results

The layouts presented in Figure 24 and Figure 26 have been fabricated in the Andrew Electromagnetic Laborarory at UIC using a CNC machine on a Roger RO4003C substrate with dielectric thickness of 32 mil (0.813 mm), dielectric constant of $\epsilon_r = 3.55$ and copper layer thickness of 35 μm. The manufactured prototypes with the 50 Ω ports are shown in Figure 28a and Figure 28b.

The structures have been measured in the UIC Andrew Electromagnetic Lab using a Keysight PNA N5222A vector network analyzer as shown in figure Figure 29. The obtained results are shown in Figure 30 and Figure 31.

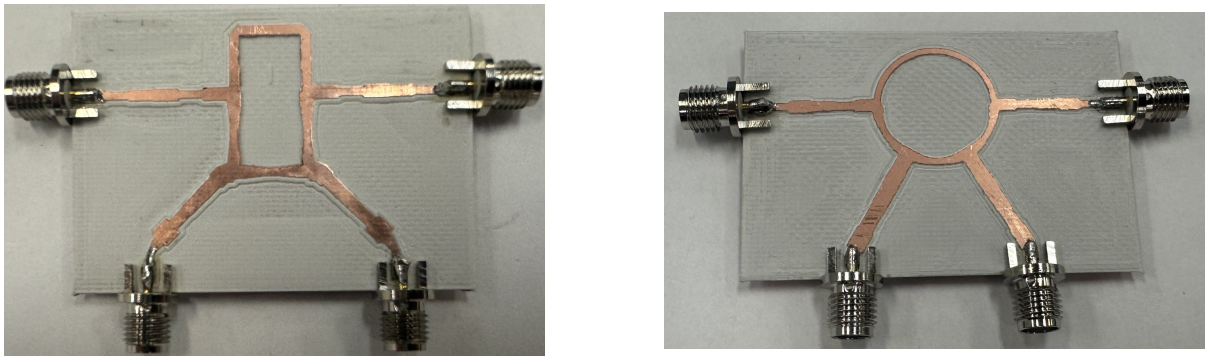

(a) (b)

Figure 28: Manufactured prototypes of the rectangular layout (a) and of the circular layout (b)

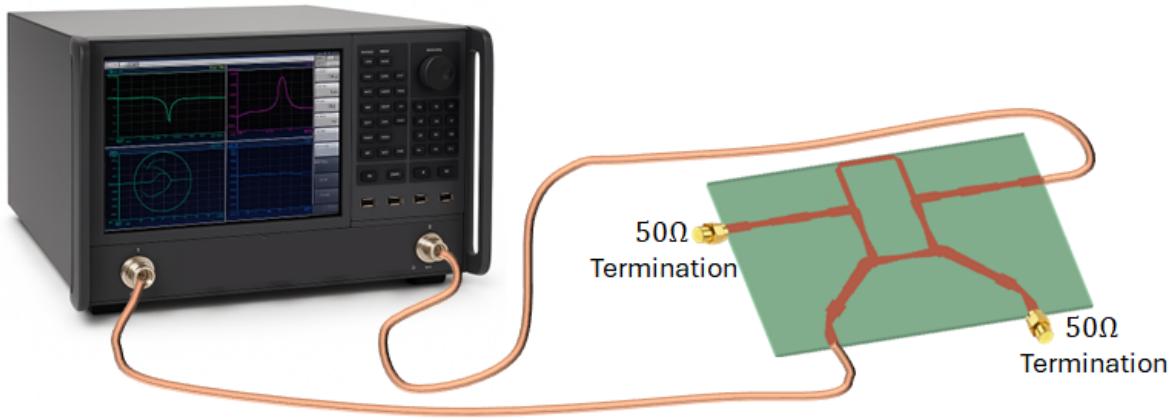

Figure 29: Measurement setup

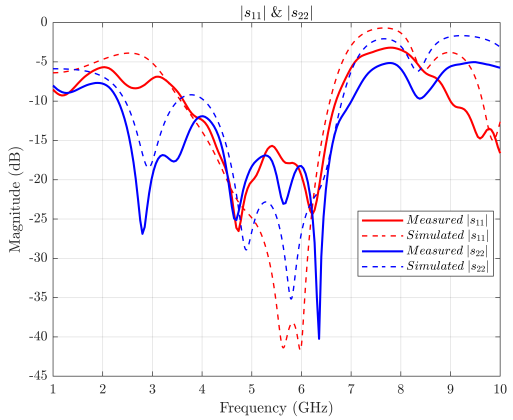

(a)

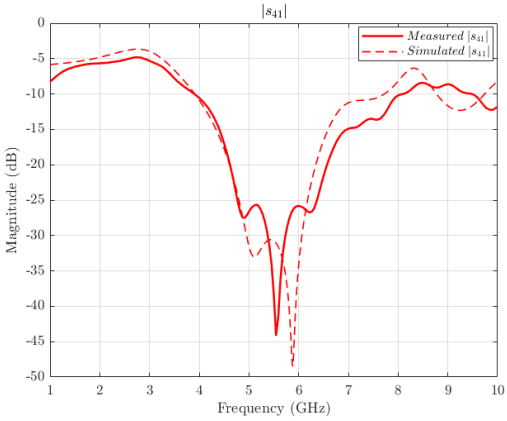

(b)

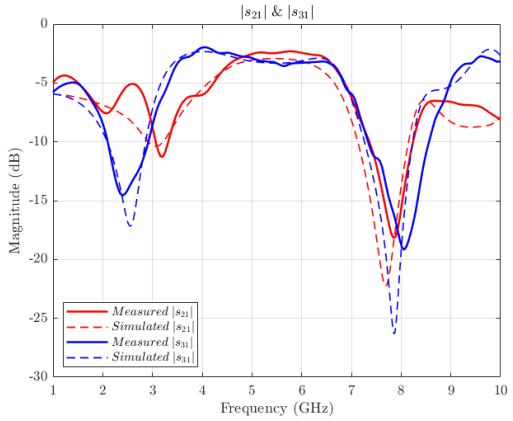

(c)

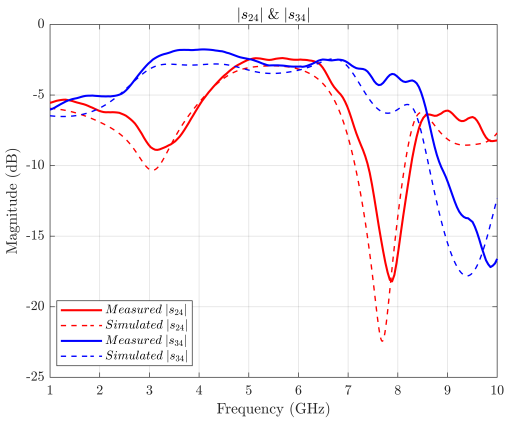

(d)

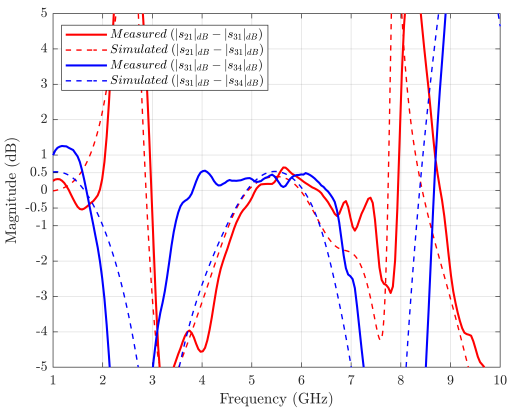

(e)

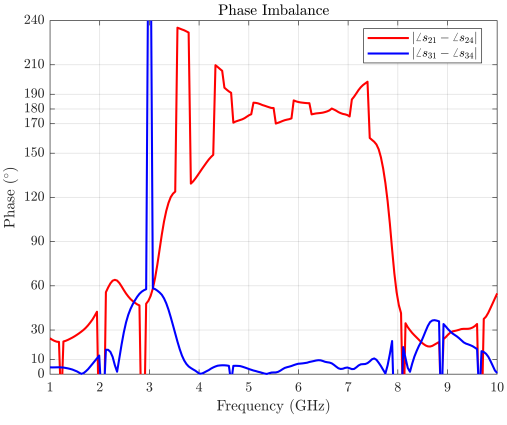

(f)

Figure 30: Measurement results of the microstrip rectangular rat-race coupler

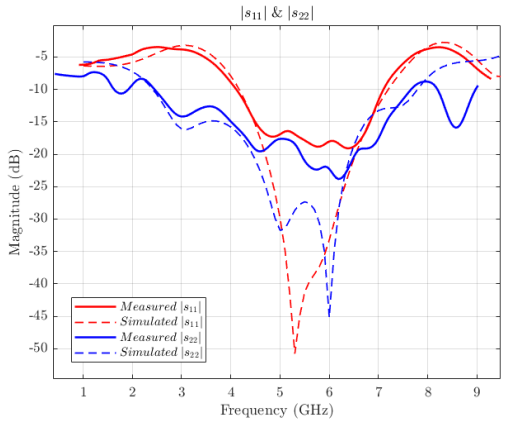

(a)

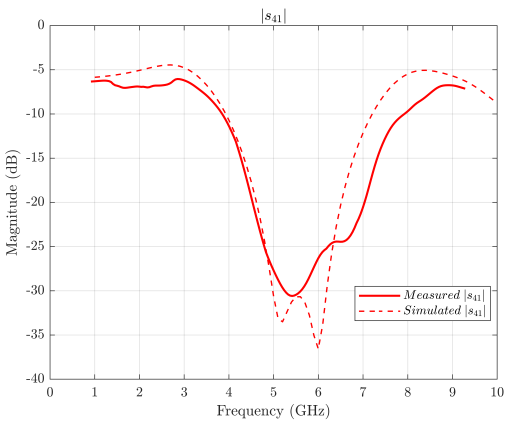

(b)

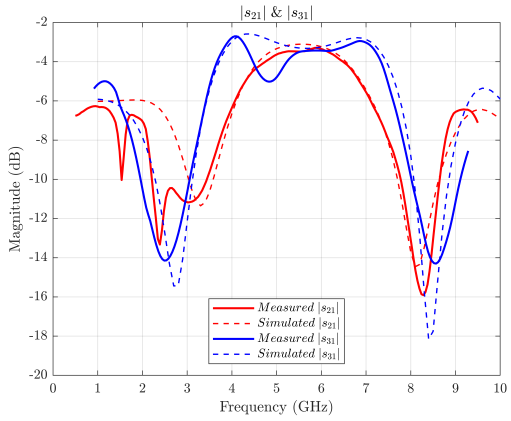

(c)

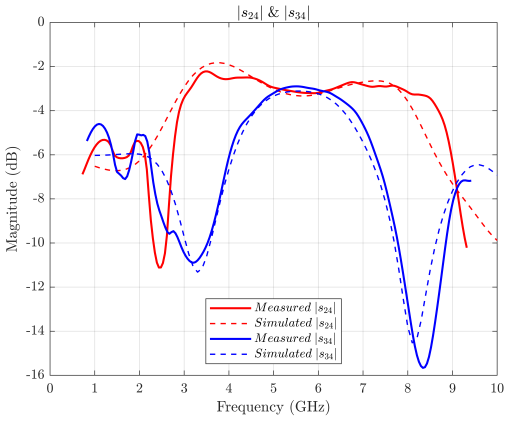

(d)

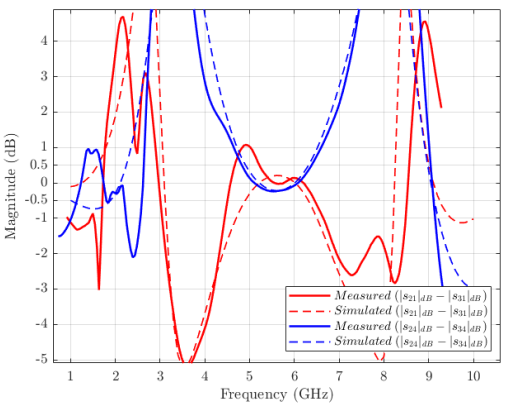

(e)

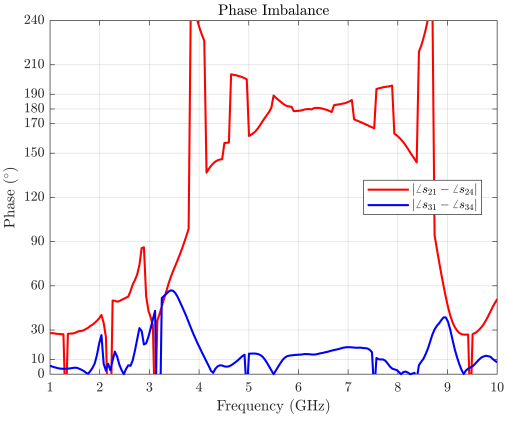

(f)

Figure 31: Measurement results of the microstrip circular rat-race coupler

4.2 Conclusions

In this work, the design of a rat-race coupler for SIC in IBFD systems has been discussed. Most of the work focused on enhancing the isolation level and bandwidth of the component to prevent the non-ideal behavior of the rat-race ring from having a detrimental effect on the overall cancellation performance. To achieve this, the novelty is implementing multisection transformers in both specific branches of the rat-race coupler and in the sections connecting the ports to the ring. The component has been implemented in microstrip using Keysight ADS, and both a circular and rectangular layout have been generated.. After the EM simulations and multiple iterations of layout optimization, the two layouts have been finally manufactured and measured at the UIC Andrew Electromagnetic laboratory facilities.

In the rectangular layout, measurement results show a reduced range where the isolation is below 30dB; however, the -25 dB band appears increased by 200 MHz compared to the EM simulation results, with a 1.5 GHz bandwidth between 4.85 GHz and 6.35 GHz. The operational range within the the phase and amplitude imbalances remain acceptable is almost the same range of the EM simulation, although worse matching performance is observed, with s_{11} and s_{22} both below -15 dB within 4.35 GHz and 6.5 GHz ($BW = 2.15$ GHz).

The measurements on the circular structure appear slightly worse than the EM simulation. The main reason for this is that a Cartesian CNC has been used to fabricate the component; as a result, the circular structure has been approximated as a sequence of straight lines, and the combination of this with the inherent manufacturing tolerances contributed to the performance degradation. Nevertheless, a broadband matching is still achieved, with s_{11} remaining below

the -15 dB band within 4 GHz and 7 GHz, while s_{22} stays within the -15 dB band within 4 GHz and 7.8 GHz. The isolation remains within the -25 dB range between 5.23 GHz and 6.35 GHz, and the range of acceptable amplitude imbalance is between 5.5 GHz and 7 GHz.

Overall, the results validate the effectiveness of the proposed multisection design to improve the isolation and bandwidth of the rat-race coupler in IBFD applications.

4.3 Future Research Directions

This section aims to suggest outlooks for future research on improving rat-race combiners in IBFD systems for SIC. The work carried out in this thesis achieved significant advancements in terms of isolation and operational bandwidth of the component; however, the solution proposed has been significantly influenced by the necessity to simplify fabrication and meet manufacturing constraints.

Relaxing these limitations would enable exploring other solutions, such as integrating coupled lines in the branches of the ring. Any signal propagating in coupled transmission lines is a combination of two distinct modes, namely even mode and odd mode, each with different characteristic impedance and effective permittivity, leading to different phase velocities and propagation constants. Combined with the capability of coupled lines to act as a multisection transformer, this dual behavior results in a smoother, more gradual variation of the phase over frequency compared to a conventional transmission line.

This property is particularly advantageous in rat-race rings, in which performance degrades due to the frequency-dependent variation of the electrical length of the branches. The implementation of coupled line, especially in the $3\lambda/4$ branch responsible for the generation of the critical 180° phase shift, would improve both the operational bandwidth and isolation of the component. Such a structure would require precise fabrication with low uncertainty, mainly due to the inherent sensitivity of coupled lines whose coupling strongly depends on the spacing between the two lines.

CITED LITERATURE

1. Noh, G., Wang, H., Shin, C., Kim, S., Jeon, Y., Shin, H., Kim, J., and Kim, I.: Enabling technologies toward fully lte-compatible full-duplex radio. IEEE Communications Magazine, 55(3):188–195, 2017.

2. Erricolo, D., Filipovic, D. S., Haneda, K., and Zhang, Z.: Guest editorial special issue on antennas and propagation aspects of in-band full-duplex applications. IEEE Transactions on Antennas and Propagation, 69(11):7085–7091, 2021.

3. Smida, B., Wichman, R., Kolodziej, K. E., Suraweera, H. A., Riihonen, T., and Sabharwal, A.: In-band full-duplex: The physical layer. Proceedings of the IEEE, 112(5):433–462, 2024.

4. Withington, T.: Band on the run: In-band full-duplex communications in military applications. Armada International, May 2024.

5. Riihonen, T. and Wichman, R.: In-band full-duplex radio transceivers: A paradigm shift in tactical communications and electronic warfare. IEEE Communications Magazine, 55(10):30–36, 2017.

6. Wang, R., Gu, Y., Chen, H., Li, Y., and Vucetic, B.: On the age of information of short-packet communications with packet management. In 2019 IEEE Global Communications Conference (GLOBECOM), pages 1–6, 2019.

7. You, X., Wang, C.-X., Huang, J., Gao, Y., Zhang, Z., Wang, M., Huang, Y., and Ai, B.: Towards 6g wireless communication networks: vision, enabling technologies, and new paradigm shifts. Science China Information Sciences, 64(1):110301, 2021.

8. Bharadia, D., McMilin, E., and Katti, S.: Full duplex for next generation of 802.11. In Proceedings of the ACM SIGCOMM 2013 Conference, pages 163–174. ACM, 2013.

9. Erricolo, D., Smida, B., Chen, P.-Y., Rastgordani, A., Pav, M., Presta, F., Kolodziej, K. E., Werner, D., Zhang, Z., Balasubramanian, M., and Das, A.: In-band full-duplex: A review and an outlook of what is enabled by electromagnetics, antennas, and propagation. Invited paper submitted to the inaugural issue of the *IEEE Journal of Special Topics in Electromagnetics, Antennas and Propagation*, 2025.

CITED LITERATURE (continued)

10. Khaledian, S., Farzami, F., Smida, B., and Erricolo, D.: Inherent self-interference cancellation at 900 mhz for in-band full-duplex applications. In 2018 IEEE 19th Wireless and Microwave Technology Conference (WAMICON), pages 1–4, Sand Key, FL, USA, April 2018.

11. Khaledian, S., Farzami, F., Smida, B., and Erricolo, D.: Robust self-interference cancellation for microstrip antennas. IEEE Transactions on Antennas and Propagation, 66(10):5574–5579, October 2018.

12. Khaledian, S., Farzami, F., Smida, B., and Erricolo, D.: A power-efficient implementation of in-band full-duplex communication system (reflectfx). In 2016 International Symposium on Signal, Image, Video and Communications (ISIVC), pages 242–246, 2016.

13. Khaledian, S., Farzami, F., Erricolo, D., and Smida, B.: A full-duplex bidirectional amplifier with low dc power consumption using tunnel diodes. IEEE Microwave and Wireless Components Letters, 27(12):1125–1127, December 2017.

14. Smida, B., Khaledian, S., Farzami, F., Islam, M. A., and Erricolo, D.: Full-duplex communications antennas. In Encyclopedia of RF and Microwave Engineering, ed. C. T. Rodenbeck. Wiley, 2nd edition, December 2024.

15. Khaledian, S., Farzami, F., Smida, B., and Erricolo, D.: Inherent self-interference cancellation for in-band full-duplex single-antenna. IEEE Transactions on Microwave Theory and Techniques, 66(6):2842–2850, June 2018.

16. Smida, B., Erricolo, D., Khaledian, S., and Farzami, F.: Self-interference cancellation for in-band full duplex single antenna communication systems. US Patent US11356235B2, June 2022. US Patent No. 11,356,235.

17. Rozhkova, A., Stutts, A. C., and Erricolo, D.: Investigation of feeding, shaping, and stacking techniques on circularly polarized patch antennas. In USNC-URSI National Radio Science Meeting, pages 88–89, Boulder, CO, USA, January 2023.

18. Stutts, A. C., Rozhkova, A., Khaledian, S., Farzami, F., and Erricolo, D.: Enhanced self-interference cancellation in a dual-fed circularly polarized antenna array via hybrid and quadrature coupling. In USNC-URSI National Radio Science Meeting, pages 98–99, Boulder, CO, USA, January 2023.

CITED LITERATURE (continued)

19. Rastgordani, A., Rozhkova, A., and Erricolo, D.: New enhancement of self-interference cancellation for circularly polarized patch antennas. In IEEE International Symposium on Antennas and Propagation and ITNC-USNC-URSI Radio Science Meeting, Florence, Italy, July 2024.

20. Rastgordani, A., Pav, M., and Erricolo, D.: Wideband self-interference cancellation circularly polarized patch array antenna. In 2025 IEEE International Symposium on Antennas and Propagation and North American Radio Science Meeting, Ottawa, Canada, July 2025. In publication.

21. Rastgordani, A., Ren, Y., Pav, M., Presta, F., Chen, P.-Y., and Erricolo, D.: Narrowband and wideband self-interference cancellation for in-band full-duplex circularly polarized microstrip array antennas. Submitted to *IEEE Transactions on Antennas and Propagation*, 2025.

22. Pozar, D. M.: Microwave Engineering. John Wiley & Sons, 5th edition, 2021.

23. European Telecommunications Standards Institute (ETSI): EN 300 328 V2.2.1: Wideband transmission systems; Data transmission equipment operating in the 2.4 GHz band; Harmonised Standard for access to radio spectrum. Technical Report EN 300 328 V2.2.1, ETSI, April 2019. Available at ETSI website.

24. European Telecommunications Standards Institute (ETSI): EN 301 893 V2.2.0: 5 GHz RLAN; Harmonised Standard for access to radio spectrum. Technical Report EN 301 893 V2.2.0, ETSI, November 2023. Available at ETSI website.

25. 3rd Generation Partnership Project (3GPP): TS 38.101-1: NR; User Equipment (UE) radio transmission and reception; Part 1: Range 1 Standalone. Technical Specification 38.101-1, 3GPP, 2024. Available online at the 3GPP website.

26. 3rd Generation Partnership Project (3GPP): TS 38.101-2: NR; User Equipment (UE) radio transmission and reception; Part 2: Range 2 Standalone. Technical Specification 38.101-2, 3GPP, 2024. Available online at the 3GPP website.

27. Jain, M., Choi, J. I., Kim, T., Bharadia, D., Seth, S., Srinivasan, K., Levis, P., Katti, S., and Sinha, P.: Practical, real-time, full duplex wireless. In Proceedings of the 17th Annual International Conference on Mobile Computing and Networking (MobiCom), pages 301–312. ACM, 2011.

CITED LITERATURE (continued)

28. Duarte, M., Dick, C., and Sabharwal, A.: Experiment-driven characterization of full-duplex wireless systems. IEEE Transactions on Wireless Communications, 11(12):4296–4307, 2012.

29. Matthaei, G. L., Young, L., and Jones, E. M. T.: Microwave Filters, Impedance-Matching Networks, and Coupling Structures. Dedham, Mass., Artech House, 1980.

30. Klopfenstein, R. W.: A transmission line taper of improved design. Proceedings of the IRE, 44(1):31–35, 1956.

31. Welch, B. L. and Sussman-Fort, C. R.: Impedance matching: Understanding the fano limit. High Frequency Electronics, 7(1):36–40, January 2008.

32. Fano, R. M.: Theoretical limitations on the broadband matching of arbitrary impedances. Technical Report Technical Report No. 41, MIT Research Laboratory of Electronics, 1948.

33. Reed, J. and Wheeler, G.: A method of analysis of symmetrical four-port networks. IRE Transactions on Microwave Theory and Techniques, 4(4):246–252, 1956.

34. Hammerstad, E. O. and Jensen, O.: Accurate models for microstrip computer-aided design. In IEEE MTT-S International Microwave Symposium Digest, pages 407–409, 1980.

35. Kirschning, M. and Jansen, R. H.: Accurate wide-range design equations for the frequency-dependent characteristics of microstrip lines. IEEE Transactions on Microwave Theory and Techniques, 32(1):83–90, January 1984.

36. Ghione, G. and Pirola, M.: Microwave Electronics. The Cambridge RF and Microwave Engineering Series. Cambridge University Press, 2017.

37. Collin, R. E.: Transmission Lines and Waveguides, pages 71–219. Wiley-IEEE Press, 2nd edition, 2001.

VITA

NAME	Francesco Presta
EDUCATION	
	Master of Science in "Electrical and Computer Engineering, University of Illinois at Chicago, May 2025, USA
	Specialization Degree in "Electronic Engineering", Jul 2025, Polytechnic of Turin, Italy
	Bachelor's Degree in "Electronic Engineering", Jul 2023, University of Calabria, Italy
LANGUAGE SKILLS	
Italian	Native speaker
English	Full working proficiency
	2020 - Cambridge Assessment English C1
	2023 - IELTS examination (7.5/9.0)
	A.Y. 2024/25 One Year of study abroad in Chicago, Illinois
	A.Y. 2023/24. Lessons and exams attended exclusively in English
Spanish	Intermediate
	Instituto Cervantes DELE B1
SCHOLARSHIPS	
Fall 2024	Italian scholarship for TOP-UIC students

ACADEMIC PUBLICATIONS

Danilo Erricolo, Besma Smida, Pai-Yen Chen, Amin Rastgordani, Mohamadreza Pav, Francesco Presta, Kenneth E. Kolodziej, Douglas Werner, Zhijun Zhang, Manushanker Balasubramanian, and Arkaprovo Das, *"In-Band Full-Duplex: A Review and an Outlook of What is Enabled by Electromagnetics, Antennas, and Propagation,"* invited paper, in publication in the inaugural issue of the *IEEE Journal of Special Topics in Electromagnetics, Antennas and Propagation*, 2025.

Amin Rastgordani, Yichong Ren, Mohammadreza Pav, Francesco Presta, Pai-Yen Chen, and Danilo Erricolo, *"Narrowband and Wideband Self-Interference Cancellation for In-Band Full-Duplex Circularly Polarized Microstrip Array Antennas,"* submitted to the *IEEE Transactions on Antennas and Propagation*, 2025.